Geochronological framework and ore genesis of the Tiantangshan Rb-Sn-W deposit, northeastern Guangdong, south China: Constraints from cassiterite and monazite U-Pb dating

Hong-Wei Peng [a,b], Hong-Rui Fan [b,c,d,*], Rong-Qing Zhang [e], Ting-Guang Lan [f]

[a] *Key Laboratory of Metallogenic Prediction of Nonferrous Metals and Geological Environment Monitoring (Ministry of Education), School of Geosciences and Info-Physics, Central South University, Changsha 410083, China*
[b] *Key Laboratory of Mineral Resources, Institute of Geology and Geophysics, Chinese Academy of Sciences, Beijing 100029, China*
[c] *College of Earth and Planetary Sciences, University of Chinese Academy of Sciences, Beijing 100049, China*
[d] *Innovation Academy for Earth Science, Chinese Academy of Sciences, Beijing 100029, China*
[e] *State Key Laboratory for Mineral Deposits Research, School of Earth Sciences and Engineering, Nanjing University, Nanjing 210093, China*
[f] *State Key Laboratory of Ore Deposit Geochemistry, Institute of Geochemistry, Chinese Academy of Sciences, Guiyang 550081, China*

ARTICLE INFO

ABSTRACT

The newly discovered Tiantangshan Rb-Sn-W deposit in the northeastern Guangdong is one of the largest Rb deposit in China. The deposit is hosted by volcanic rocks and characterized by hydrothermal mineralization of Rb and Sn-W, with minor Rb mineralization of granitic K-feldspar alteration. In this study, we conducted LA-ICP-MS U-Pb dating of cassiterite and monazite to constrain the ore-forming ages of Sn and Rb. Two stages of cassiterite (Cst) are developed in the wolframite-cassiterite quartz vein, and the Cst I and Cst II yielded weighted mean $^{206}Pb/^{238}U$ ages of 133.9 ± 2.0 Ma and 133.2 ± 1.6 Ma, respectively. Monazites from biotite quartz vein yielded weighted mean $^{206}Pb/^{238}U$ ages of 134.2 ± 1.8 Ma and 132.7 ± 1.1 Ma. Combined with previous studies, a geochronological framework of volcanic eruptions (ca. 137 Ma), alkali feldspar granite (ca. 136 Ma) and Rb-Sn mineralization (134 to 133 Ma) for the deposit was established. Thus, the Rb-Sn-W mineralization is genetically related to the alkali feldspar granite and a volcanic-intrusive connection. Most Rb resources of the deposit are hosted by hydrothermal biotite in biotite quartz vein and related biotite alteration of volcanic wall rocks. Meanwhile, the K-feldspar alteration of the alkali feldspar granite displays higher Rb contents (1992–2092 ppm), stronger REE tetrad effect and lower Zr/Hf, Nb/Ta and Y/Ho ratios than the unaltered granite, indicating important involvement of hydrothermal fluids in this type of Rb enrichment. In combination with recent age data, the Tiantangshan deposit, with Yanbei and Taoxihu in the southeastern Jiangxi, are related to the numerous Sn deposits in southeastern Guangdong, which together form an early Cretaceous Sn metallogenic belt in South China. The early Cretaceous Sn belt was formed under an extensional environment likely due to the roll back of the subducted paleo-Pacific plate. The Tiantangshan deposit is indicative of Sn and related rare-metal exploration potential in the early Cretaceous volcanic basins in adjacent areas.

1. Introduction

South China, particularly the Nanling Range, is one of the most important W-Sn metallogenic province in the world, and also renowned by rare-metal mineralization, like Nb, Ta, Li and Be (e.g., Chen et al., 2008; Mao et al., 2013; Wang et al., 2020). The large-scale W-Sn and rare-metal mineralization are genetically associated with the Yanshanian extensive tectono-magmatism, that was formed under intra-continental extensional setting in response to the paleo-Pacific subduction (e.g., Zhou et al., 2006; Li and Li, 2007; Mao et al., 2013; Ni et al., 2021). Noticeably, the Nanling Range is also the most important Rb resource region in China (Sun et al., 2019). Rubidium is a rare-metal element, and is usually listed as a critical metal by numerous countries due to its excellent photovoltaic performance in perovskite solar cells (Saliba et al., 2016) and wide applications in information technology, medical industry and electronics, etc (Sun et al., 2019). In the

---

Nanling Range, one important geological feature for the Rb mineralization is that it is commonly concomitant with W-Sn mineralization. In the system, Rb mineralization is commonly restricted in highly differentiated granitoid and associated pegmatite by incorporating into micas and K-feldspar (Černý et al., 2003; Sun et al., 2019), whereas, the W-Sn mineralization is commonly present as quartz veins developed in the roof of the granitic plutons (e.g., Wang et al., 2020; Ni et al., 2021). However, there is still with poor understanding on the genetic relationship between the mineralization of Rb and Sn-W, and the role of hydrothermal fluids in Rb enrichment.

Tiantangshan is a newly-discovered deposit that has been explored to have resources of ca. 170 kt Rb_2O, 5050 t Sn and 4800 t WO_3, with a small amount of Pb (2600 t) and Zn (240 t). Accordingly, the Tiantangshan is a Rb-dominated polymetallic (Rb-Sn-W) deposit, and one of the largest Rb deposit in China (Sun et al., 2019). One remarkable mineralized feature of the Tiantangshan deposit is that the most Rb resource is of hydrothermal origin, which is hosted by hydrothermal biotite in quartz veins (Han et al., 2021), and meanwhile, a small amount of Rb resource is restricted in granitic systems. However, there remains ambiguous to the genetic relations between the hydrothermal Sn-W and Rb mineralization, and the two types of Rb mineralization. The Tiantangshan deposit is situated in the eastern Nanling Range. However, different from the W-Sn and rare metal mineralization of the Nanling Range concentrated in late Jurassic, it was likely formed during early Cretaceous inferred from previous zircon U-Pb studies of granitic rocks (Jia et al., 2019; Peng et al., 2021). In addition, the Tiantangshan deposit is situated in a volcanic basin, and previous zircon U-Pb dating suggested that the ore-related granite is coeval with the volcanic rocks that serve as the wall rocks of the granite and related hydrothermal mineral systems, which imply a possible volcanic-intrusive connection (Wu et al., 2011; Jia et al., 2019; Peng et al., 2021). These geological and mineralization features are all suggestive of the uniqueness of the deposit, however, its significance and implication for regional metallogenesis are still unclear. Precise ore-forming ages are crucial for interpreting the genetic relationship among the different types of mineralization and the region metallogenic implications of the deposit, which is still lacking.

The development of *in-situ* isotopic dating technologies makes accurate estimation of ore-forming age feasible and reliable. Cassiterite is the key ore mineral of Sn mineralization, and recently, numerous studies have confirmed that LA-ICP-MS cassiterite U-Pb dating is a reliable and direct estimation for Sn mineralization age (e.g., Li et al., 2016; Zhang et al., 2017; Cheng et al., 2019). In addition, monazite is a common accessory mineral in granitic-hydrothermal system, and the *in-situ* U-Pb dating of which has been shown to be effective in constraining age of hydrothermal mineralization (e.g., Rasmussen et al., 2006; Williams et al., 2007; Ma et al., 2017; Deng et al., 2020).

In this study, we examined detailed geology, mineral paragenesis and geochemistry of the Tiantangshan deposit, and carried out LA-ICP-MS U-Pb dating of hydrothermal cassiterite and monazite to establish the geochronological framework and genetic model of the deposit, and further to decipher its implications on W-Sn and rare-metal mineralization of the South China.

2. Regional geological background

The Tiantangshan deposit (latitude 24°41′ N, longitude 115°22′ E) is located in the Mabugang basin, eastern Nanling Range, Cathaysia block (Fig. 1b). The Cathaysia block, a major geological body in the southeast China, was sutured with the Yangtze block in the northwest along the Jiangnan orogen during Neoproterozoic (Fig. 1a; Zhao and Cawood, 2012). The Cathaysia block contains Precambrian basement rocks that are mainly Paleoproterozoic and Neoproterozoic in age (Zhao and Cawood, 2012), and is developed with multiple periods of tectono-magmatism from Paleozoic to Mesozoic (e.g., Zhou et al., 2006). Especially, during middle-late Mesozoic (namely Yanshanian period), a huge mass of granitic and volcanic rocks were formed in the Cathaysia block, which was commonly thought to be formed under extensional
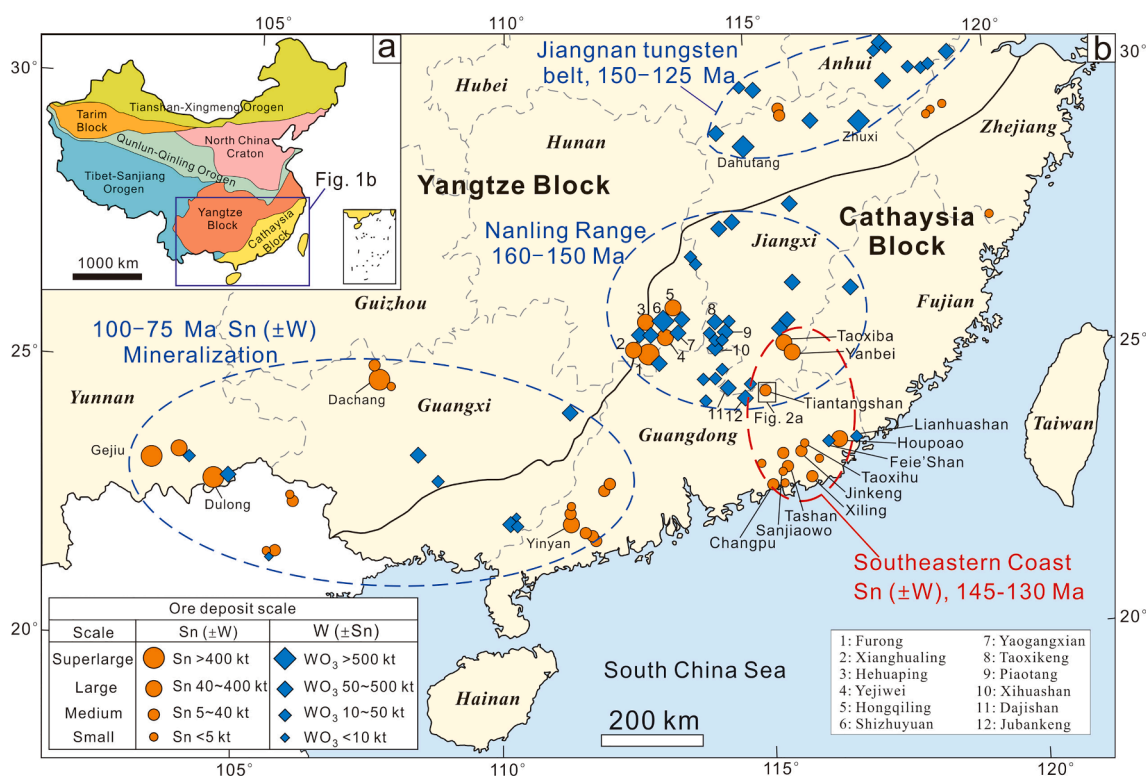

Fig. 1. Simplified maps showing major tectonic units of China (a) and distribution of major Mesozoic W-Sn deposits in South China (b) (modified after Hu et al., 2021, and references therein).

environment related to the subduction of the paleo-Pacific plate (e.g., Zhou et al., 2006; Li and Li, 2007). The Nanling Range is located in the central-western region of the Cathaysia block, and is a world-renowned W-Sn metallogenic province, in which the large-scale mineralization is predominantly genetically related to the Yanshanian granitic magmatism (e.g., Mao et al., 2007; Mao et al., 2013; Yuan et al., 2019; Wang et al., 2020). Meanwhile, the Nanling range is also an important producing region of rare-metals (e.g., Nb-Ta, Li, Be and Rb) and heavy rare earth (e.g., Mao et al., 2013; Wang et al., 2020).

The Mabugang basin, hosting the Tiantangshan deposit, is located in the southeastern part of the Nanling Range (Fig. 1b). It is a volcanic basin that covers an area of approximately 150 km², and its domain is mainly restricted by NE-, NW- and EW-trending regional faults (Fig. 2a). The basin is developed within Neoproterozoic (Sinian) basement rocks that mainly comprise migmatitic, gneissic granite and a series of *meta*-sedimentary rocks. The volcanic sequences of the basin are comprised of intermediate to acid volcanic rocks, which are dominated by trachytic-trachyandesitic welded tuff at the base and middle, which are switched to trachydacite and rhyolitic tuff at top. The volcanic sequences have been confirmed to be formed during early Cretaceous by zircon U-Pb dating (ca. 137 Ma; Wu et al., 2011; Jia et al., 2019; Peng et al., 2021). Additionally, several periods of granites, including Indosinian, early and late Yanshanian periods, are developed in adjacent areas of the basin (Fig. 2a). In the Mubugang basin, Tiantangshan is the most valuable deposit, and several deposits mainly occur in the peripheries of the basin, like the Jinshizhang silver deposit (Fig. 2a).

3. Geology of the Tiantangshan deposit

3.1. Geological framework

The Tiantangshan Rb-Sn-W polymetallic deposit is situated in the western area of the Mabugang volcanic basin, where the caldera structure is developed (Fig. 2a; Guo, 2009). The polymetallic mineralization of the deposit is genetically associated with an alkali feldspar granite that occurs as a stock intruding into the volcanic sequences of the Mabugang basin (Fig. 2c). The granite shows flesh pink color with medium-fine grained texture, and mainly consists of quartz (30 to 40 vol %), alkali feldspar (perthite and microcline, 40 to 50 vol%), plagioclase (ca. 10 vol%) and biotite (ca. 10 vol%) (Fig. 3a). It is characterized by high silica (73.9 to 77.0 wt%) and alkali ($K_2O + Na_2O$ = 7.3 to 8.7 wt%), and highly evolved geochemical features (e.g., "seagull-like" REE pattern, marked depletion of Sr, Ba, P and Ti) (Peng et al. 2021). The volcanic sequences of Mabugang basin are served as the wall rocks of the granite and related polymetallic mineralization, with three lithological units identified at surface (Fig. 2b). Trachyte-trachyandesite is developed at the central region of the deposit and is the major wall rock of the granite and mineralization (Fig. 2b, 2c). The alkali feldspar granite (ca. 136 Ma) has been confirmed to be with consistent ages with the three volcanic units (ca. 137 Ma; Peng et al., 2021).

Hydrothermal alterations are pervasive in the Tiantangshan deposit, which mainly include greisenization and K-feldspar alteration of the granite, and hornfelsic and biotite alteration of the volcanic wall rocks. The greisen is developed at the roof part of the granite, and occurs as an irregular cupola with the largest thickness of ca. 250 m at the convex of

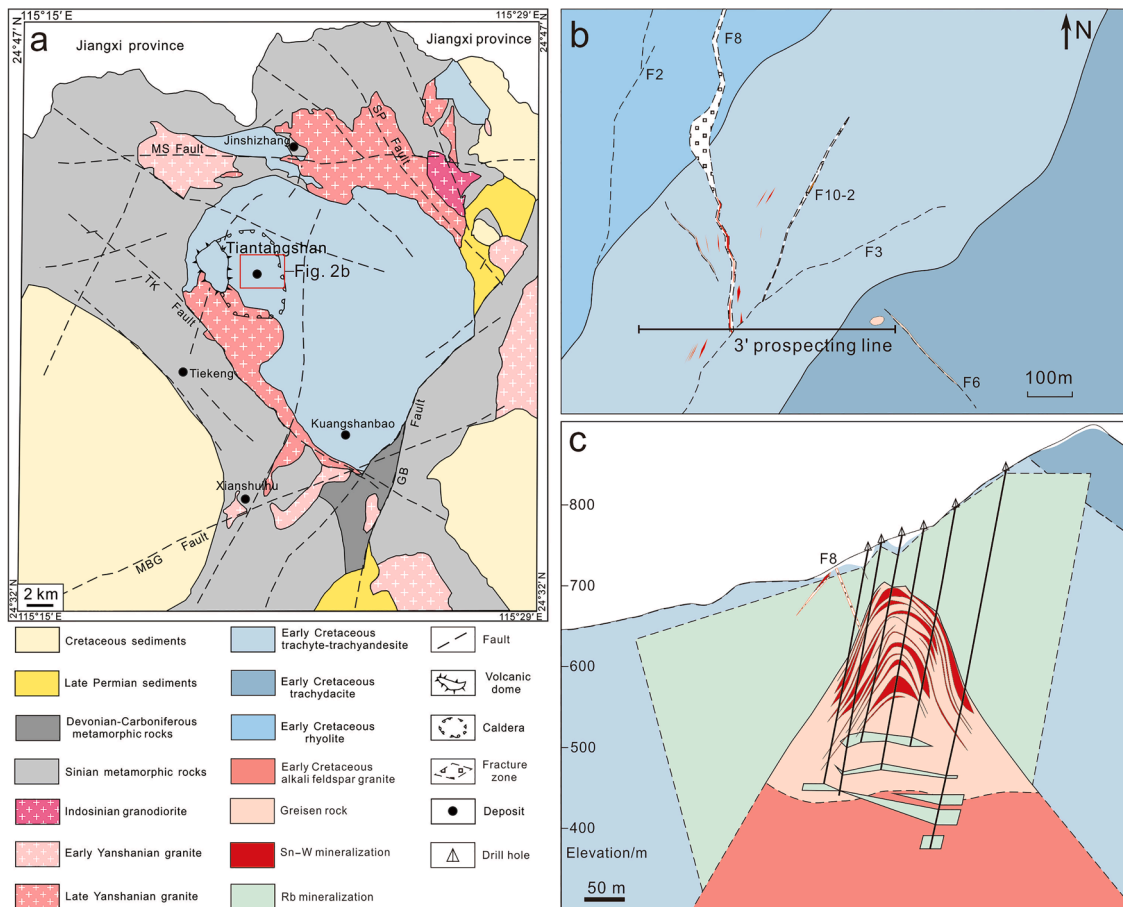**Fig. 2.** (a) Simplified geological map of the Mabugang basin and (b) the Tiantangshan deposit, modified after Guo et al. (2009). (c) Geological profile along the 3′ prospecting line in Fig. 2b. The Rb mineralization occurring in alteration zones of granite corresponds to the K-feldspar alteration. F8 and F10-2 are *syn*-mineralization faults, and F2 and F3 are post-mineralization and pre-mineralization faults, respectively.
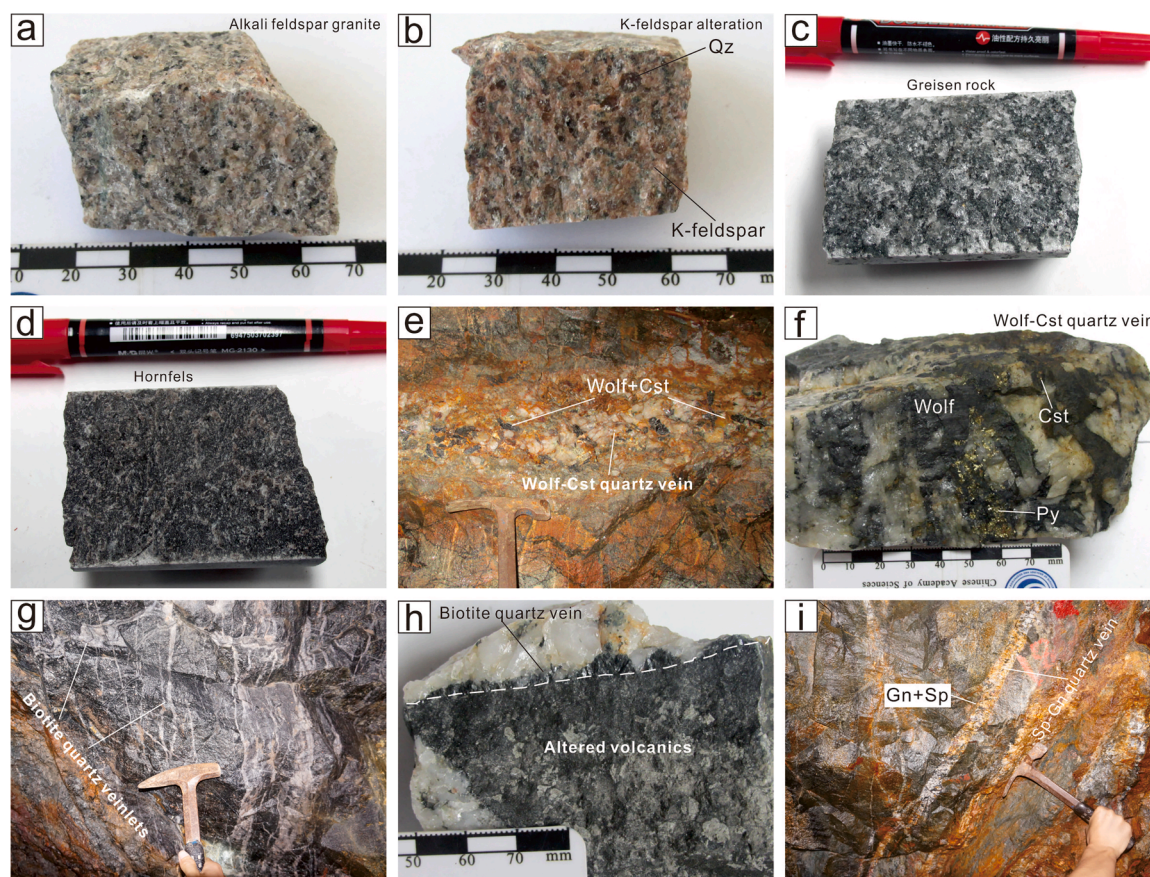
Fig. 3. Photographs of granite, alteration rocks and polymetallic mineralization of the Tiantangshan deposit. (a) Alkali feldspar granite; (b) K-feldspar alteration rock; (c) Greisen; (d) Hornfels of volcanic wall rock; (e) Sn-W ore body from tunnel; (f) typical hand specimen of wolframite-cassiterite quartz vein; (g) Rb ore body presenting as biotite quartz veinlets from tunnel; (h) typical hand specimen of biotite quartz vein and related biotite alteration of volcanic wall rocks; (i) Pb-Sn ore body from tunnel. Cst = cassiterite; Gn = galena; Py = pyrite; Qz = quartz; Sp = sphalerite; Wolf = wolframite.

the granite (3′ section line; Fig. 2c). The greisen is dominantly comprised of mica (30 to 50 vol%) and quartz (40 to 60 vol%), with variable topaz (locally up to 20 vol%) and minor pyrite (Fig. 3c). K-feldspar alteration is variably developed between the greisen and granite, which shows dark flesh pink color, and is characterized by high proportion of K-feldspar and secondary growth of quartz with globular shape with minor biotite (Fig. 2c; Fig. 3b). In the volcanic wall rocks, hornfels is developed extensively, which is characterized by dark color and aphanitic appearance (Fig. 3d). The biotite alteration is related to pervasive quartz veins cutting into the wall rocks, which is present as dense small flaky biotite spreading in the volcanic wall rocks from the quartz veins, and usually overprints the hornfels of wall rocks (Fig. 3g and h). The biotite alteration covers a large volume with variable thickness up to ca. 300 m, which largely correspond to the Rb ore bodies (Fig. 2c).

The polymetallic mineralization of Rb, Sn-W and Pb-Zn of the Tiantangshan deposit predominantly occur as quartz veins, which are biotite quartz vein, wolframite-cassiterite quartz vein and sphalerite-galena quartz vein, respectively (Fig. 3e, g, i). The different mineralization and quartz veins do not show obvious cross cutting relationship, but are distributed in different regions of the deposit (Fig. 2b and c). The biotite quartz veins are emplaced in volcanic wall rocks, which give rises to extensive biotite alteration of the wall rocks (Fig. 3g and h). Most Rb resources of the deposit are hosted by the hydrothermal biotite in the veins and the related extensive biotite alteration zones, and Rb enrichment is accomplished by substituting for K in the biotite (Han et al., 2021). These Rb ore bodies possesses an estimated reserve of 169000 t Rb_2O. In addition, few Rb resources of the deposit are hosted by the K-feldspar of the granitic K-feldspar alteration (Fig. 2c, Fig. 3b; Han et al., 2021), which give an estimated reserve of 4400 t Rb_2O. The Sn-W ore

bodies, represented by the wolframite-cassiterite quartz vein, are developed in inner contact zone between greisen and volcanic wall rocks, and volcanic wall rocks along the *syn*-mineralization faults of F8 and F10-2 (Fig. 2c; Fig. 3e). These ore bodies have an estimated reserve of 4050 t Sn and 4800 t WO_3. The Pb-Zn mineralization of the sphalerite-galena quartz vein are emplaced in shallow fractures at distal regions of volcanic wall rocks, which are estimated to be 2600 t and 240 t, respectively (Fig. 3i).

3.2. Vein and paragenetic sequences

The wolframite-cassiterite quartz vein is characterized by occurrence of cassiterite and wolframite in the veins (Fig. 3e and f). Wolframite in the veins usually occurs as relatively large crystal in tabular and columnar shape (up to centimeter level in length), whereas, cassiterite generally occurs as relatively small crystals with subhedral to anhedral shape (Fig. 3f; Fig. 4a, c and d). Noticeably, cassiterite in the veins consists of two types, including cassiterite I (Cst I) and II (Cst II). The Cst I has dark brown color and is non-luminescent and relatively uniform in texture under CL images, whereas, Cst II has light brown color and is characterized by relatively bright luminescence and oscillatory growth bands under CL images (Fig. 4e and f). The Cst II encroach into Cst I to form irregular boundaries concave to the Cst I, suggesting a later deposition of Cst II than the Cst I (Fig. 4e and f). Except for wolframite and cassiterite, numerous ore minerals of magnetite, native bismuth (Bi), bismuth sulfides and pyrite, with minor arsenopyrite, chalcopyrite, galena and sphalerite, are also developed in the quartz veins. Magnetite and pyrite usually occur at surrounding areas of wolframite, and it can be observed that pyrite and the base metal minerals intrude into
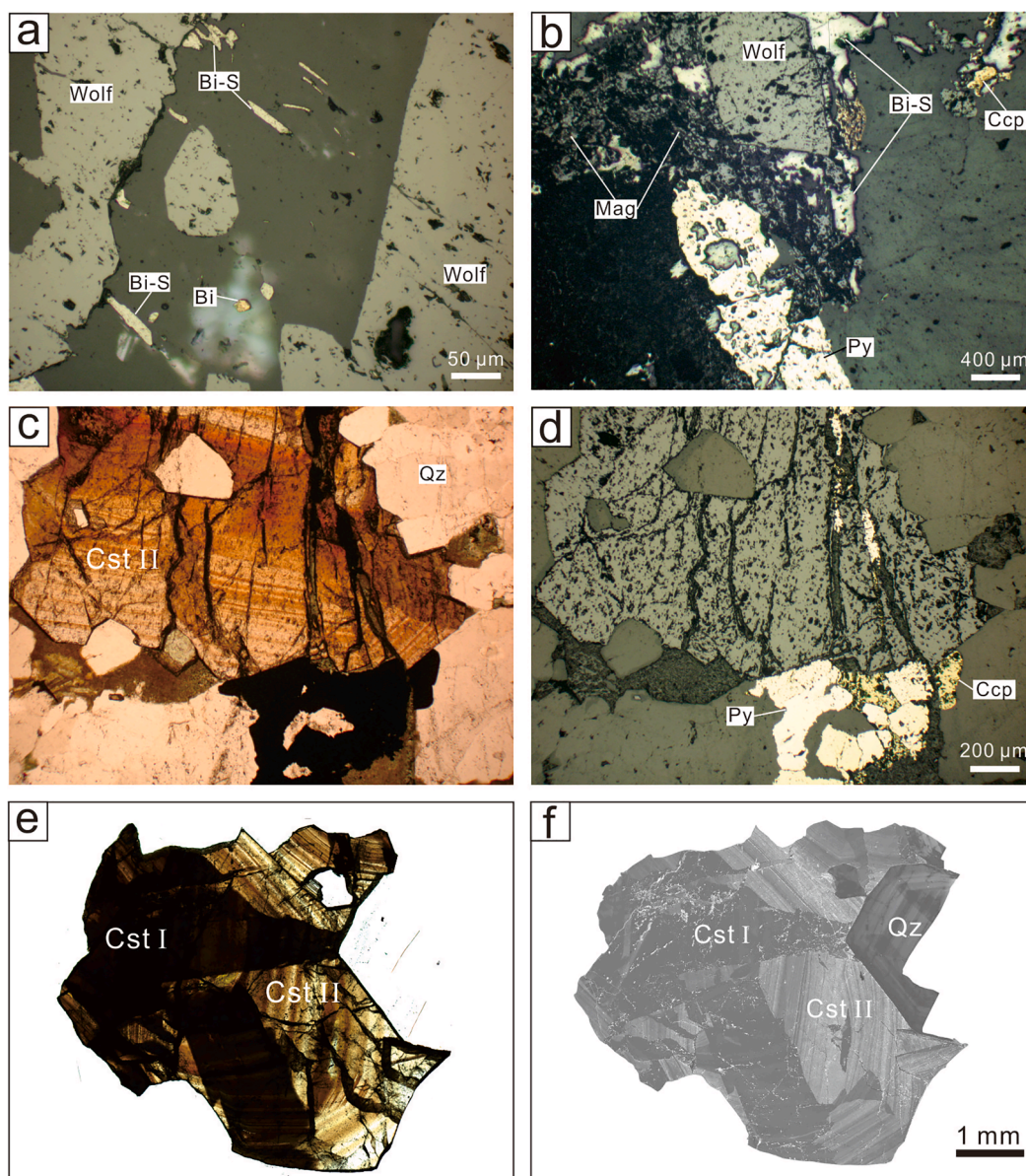
Fig. 4. Micrographs showing mineral assemblages of the wolframite-cassiterite quartz vein (a-d), and textural features of two stages of cassiterite under transmitted light (e) and SEM-CL (f). Bi = native bismuth; Bi-S = bismuth sulfide; Ccp = chalcopyrite; Cst = cassiterite; Mag = magnetite; Py = pyrite; Qz = quartz; Wolf = wolframite.

wolframite and cassiterite (Fig. 4b). Native Bi occur as globular crystals, and commonly fill in wolframite and cassiterite along micro-fractures, and are distributed in quartz with Bi-sulfide minerals (Fig. 4a and b). Inferred from their spatial relationships under petrographic observations, these minerals are deposited later than the wolframite and cassiterite in the veins.

The biotite quartz vein is marked by abundant occurrences of biotite that are hosted in the quartz and distributed in adjacent volcanic wall rocks (Fig. 3g and h). A large number of biotite are present as relatively small flaky crystals (generally <200 μm) with dark brown to light brown color, and are densely dispersed in volcanic wall rocks extending from the quartz vein walls, which leads to the biotite alteration of the wall rocks (Fig. 3h; Fig. 5a). Meanwhile, a portion of biotite occurs as relatively large flaky crystals usually larger than 500 μm, with brown green-light green to light red color, which is usually hosted in quartz and distributed along quartz vein walls (Fig. 5b). Fluorite and molybdenite are common in the veins, in which the latter is generally characterized by occurring as radial aggregations of euhedral tabular crystals (Fig. 5c).

In addition, monazite is usually observed in the biotite quartz veins, which occurs as euhedral to subhedral crystals, and generally shows oscillatory growth bands under BSE images (Fig. 5e and h). Fluorite, molybdenite and monazite are generally intergrown with the biotite, and are usually distributed along quartz vein walls and in quartz with biotite (Fig. 5c, e–g). Similar to the wolframite-cassiterite quartz vein, magnetite, Bi-sulfides, native bismuth and pyrite with little arsenopyrite, sphalerite and galena are also variably superimposed in the quartz veins. In addition, magnetite and pyrite are usually overprinted in the biotite (Fig. 5c–d). Compared to the wolframite-cassiterite quartz veins, the ratio between native Bi and Bi-sulfides in the biotite quartz vein is lower, and the Bi-sulfides are usually distributed in surrounding area of molybdenite, and in quartz (Fig. 5c).

The sphalerite-galena quartz vein is characterized by occurrences of galena and sphalerite in the veins. In this vein, except for galena and sphalerite, only minor fluorite and chalcopyrite with limited arsenopyrite and pyrite are developed (Fig. 3i).

The mineral assemblages and paragenetic sequences of the K-
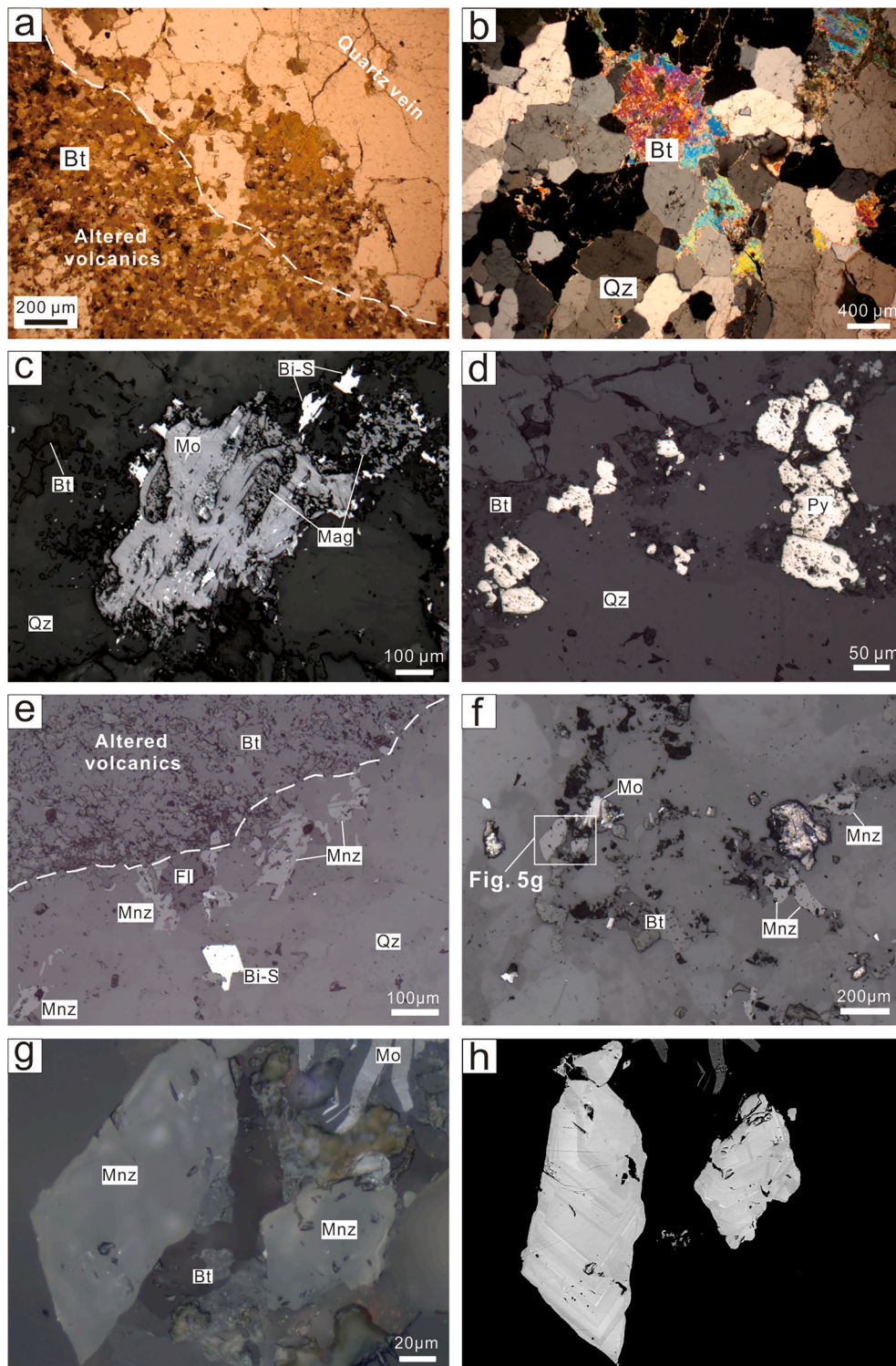
Fig. 5. Micrographs showing mineral assemblages of the biotite quartz vein (a-d), and distribution of monazite in biotite quartz vein (e-f), and detailed mineralogical features of monazite under reflected light (g) and SEM-BSE (h) from Fig. 5f. The white dotted lines in Fig. 5a and e are boundaries between quartz vein and volcanic wall rock. Bi-S = bismuth sulfide; Bt = biotite; Fl = fluorite; Mag = magnetite; Mnz = monazite; Mo = molybdenite; Qz = quartz.

feldspar alteration and different quartz veins are summarized in the Fig. 6.

4. Samples and analytical methods

Representative ore samples of the wolframite-cassiterite quartz vein, biotite quartz vein and sphalerite-galena quartz vein were collected

from drill holes of 3, 1, and 3′ prospecting lines, and from the tunnel at 671 and 711 m elevation.

4.1. Scanning electron microscope (SEM) imaging

Internal structure of cassiterite was studied by cathodoluminescence (CL) imaging using a TESCAN GAIA3 field-emission SEM at Beijing
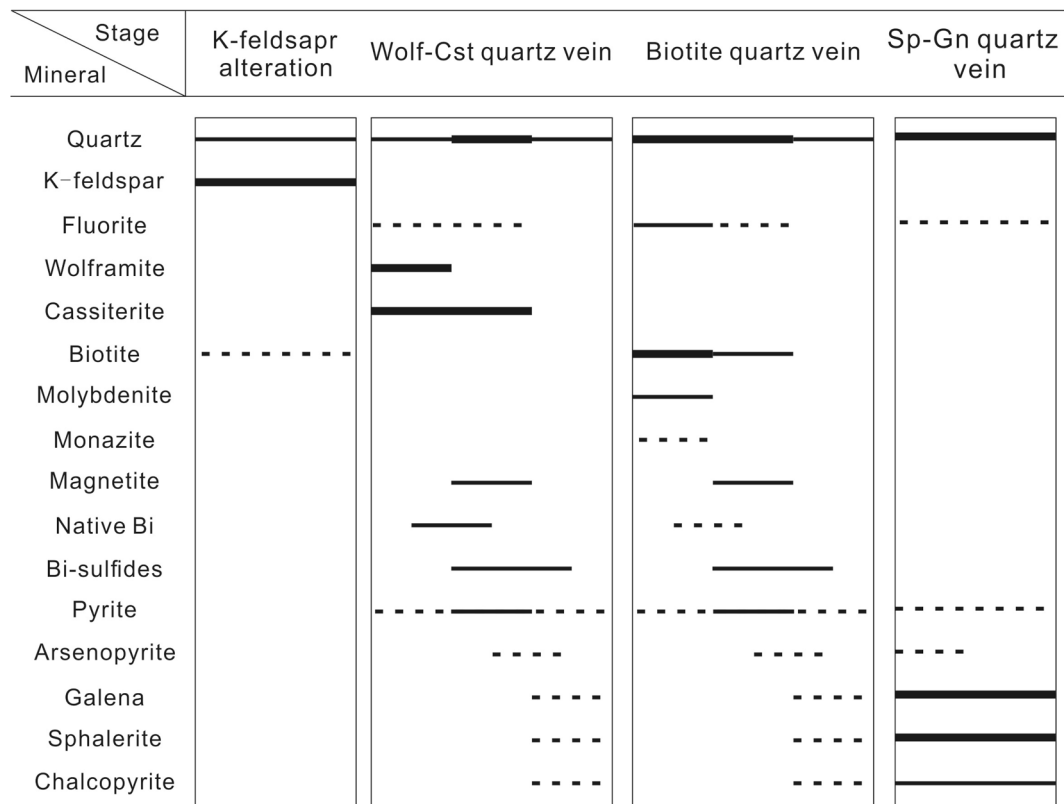
Fig. 6. Paragenetic sequence of mineralization of the Tiantangshan deposit. Cst = cassiterite; Gn = galena; Sp = sphalerite; Wolf = wolframite.

Research Institute of Uranium Geology, and the observation of monazite was carried out with backscattered electron (BSE) images by a Nova NanoSEM 450 field-emission SEM at the Institute of Geology and Geophysics, Chinese Academy of Sciences (IGGCAS).

4.2. LA-ICP-MS U-Pb dating of cassiterite

In-situ U-Pb dating of cassiterite was conducted using an Thermo Fisher ICAP QC ICP-MS equipped with an ASI RESOlution LR 193 nm ArF excimer laser at the State Key Laboratory of Mineral Deposits Research, Nanjing University. Analytical spots were carefully chosen based on optical micrographs and CL images to avoid fluid inclusion and fracture. Laser repetition of 6 Hz and energy density of 3.9 J/cm^2 were used during the analyses, with laser spot size of 67 μm. Helium gas carrying the ablated sample aerosol was mixed with argon and nitrogen (additional di-atomic gas) to enhance sensitivity, and finally flowed into the ICP-MS instrument. The NIST SRM614 was used as the external standard of ^{207}Pb/^{206}Pb and trace elements, and was analyzed twice every 12 analyses. The CLGH cassiterite, from Cornwall tin district, England, with a U-Pb age of 285.14 ± 0.25 Ma (2σ) Ma measured by ID-TIMS (Tapster and Bright, 2020), was served as the external standard of ^{238}U/^{206}Pb and was analyzed twice every 6 sample analyses. The Yankee cassiterite from the Yankee cassiterite-quartz vein related to the Mole granite, New England, eastern Australia, was employed as the monitoring standard. Nine analyzed spots of the Yankee monitoring cassiterite yielded a Tera-Wasserburg U–Pb lower intercept age of 248.1 ± 3.0 Ma (2σ; MSWD = 1.8) and a weighted mean ^{206}Pb/^{238}U age corrected by ^{207}Pb of 247.9 ± 5.9 Ma (2σ; MSWD = 0.49; Supplemental Fig. S1), which are consistent with its ID-TIMS U-Pb age of 246.48 ± 0.51 Ma (2σ; Carr et al., 2020). The detailed analytical information is seen in Zhang et al. (2017). The raw data from the ICP-MS were processed using ICPMSDataCal 10.1 (Liu et al., 2010), and the age was calculated by Isoplot 4.15 (Ludwig, 2012).

4.3. LA-ICP-MS U-Pb dating of monazite

In-situ U-Pb dating analyses of monazite by LA-ICP-MS were conducted at the State Key Laboratory of Ore Deposit Geochemistry, Institute of Geochemistry, Chinese Academy of Sciences, Guiyang, China. A GeoLasPro 193 nm ArF excimer laser system was connected to an Agilent 7500x ICP-MS instrument to acquire ion-signal intensity. Laser repetition of 5 Hz and energy density of 3 J/cm^2 were used during the analyses, with laser spot size of 16 μm. Helium was applied as a carrier gas which was mixed with Argon via a T-connector before entering the ICP-MS. Each analysis included a background acquisition of approximately 40 s (gas blank) followed by 45 s of data acquisition. Monazite of MGMH. 117531 with an age of 272 Ma (Tomascak et al., 1996) was served as external standards for U-Pb dating, which was analyzed twice every 10 sample analyses. Off-line selection of background and analytical signals, time-drift correction, and quantitative calibration were completed using ICPMSDataCal (Liu et al., 2010). Concordia diagrams and weighted mean calculations were made using Isoplot 4.15 software (Ludwig, 2012).

4.4. Whole-rock trace element analysis

Whole-rock trace element analyses were conducted at the IGGCAS. Whole-rock powders (40 mg) were dissolved in distilled HF + HNO$_3$ in Teflon capsules at 200 °C for 5 days, which were then nearly dried and dissolved with HNO$_3$ at 150 °C twice for two days. Dissolved samples were diluted to 49 ml by 1% HNO$_3$ with an addition of 1 ml 500 ppb indium as an internal standard. The trace element concentrations were determined by ICP-MS using a Finnigan MAT Element spectrometer, and the analytical uncertainties for most elements were within 5%.
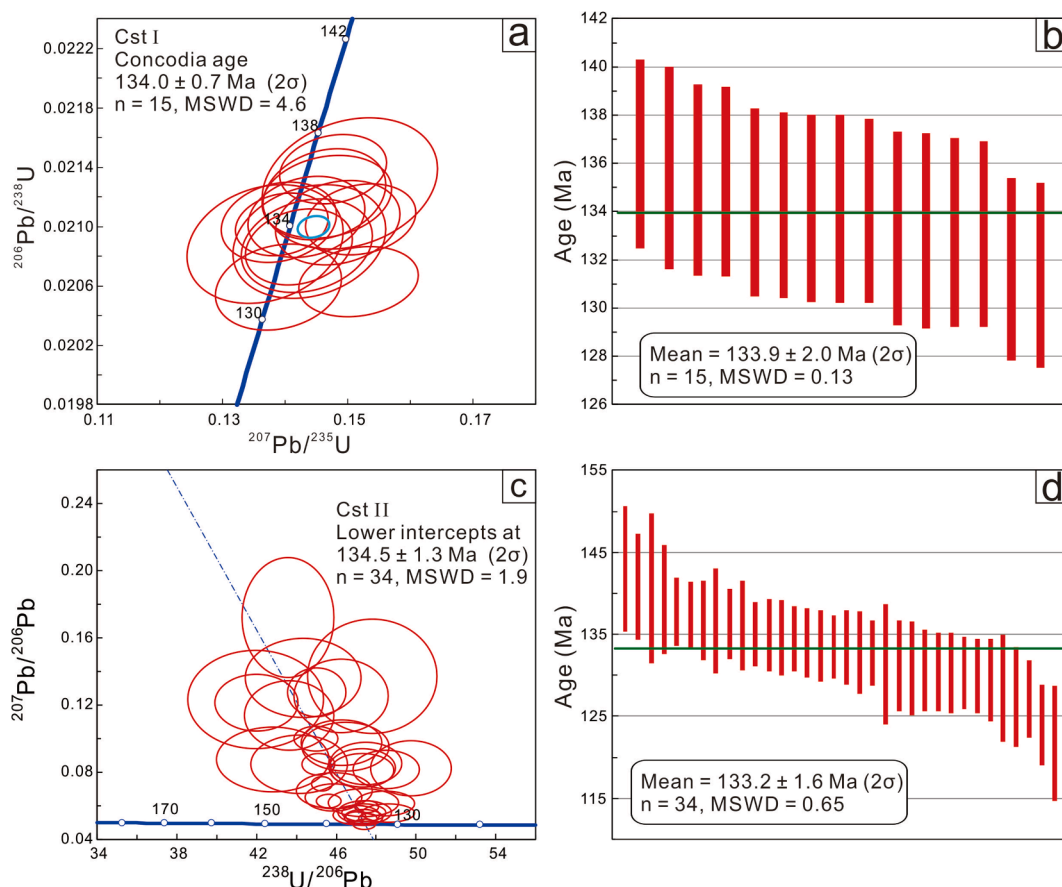
5. Results

5.1. Cassiterite U-Pb age

Two types of cassiterite from the wolframite-cassiterite quartz veins have been analyzed by LA-ICP-MS, with the results presented in Table 1. Sixteen analyzed spots of Cst I show relatively high concentrations of U (15.5 to 86.0 ppm) and low concentrations of Th ($\leq$0.02 ppm), and 15 spots of which obtained ages with $\geq$ 95% concordance, except one eliminated spot with low concordance. The 15 spots yield a concordia age of 134.0 $\pm$ 0.7 Ma (2σ; MSWD = 4.6) and a weighted mean ^{206}Pb/^{238}U age of 133.9 $\pm$ 2.0 Ma (2σ; MSWD = 0.13) (Fig. 7a and b). Thirty-four spots of Cst II were analyzed, that have variable but relatively lower contents of U (0.75 to 77.5 ppm) and relatively low contents of Th ($\leq$0.11 ppm). The analytical spots give a Tera-Wasserburg U-Pb lower intercept age of 134.5 $\pm$ 1.3 Ma (2σ; MSWD = 1.9), and the ^{207}Pb corrected data yield a weighted mean ^{206}Pb/^{238}U age of 133.2 $\pm$ 1.6 Ma

(2σ; MSWD = 0.65) (Fig. 7c-d).

5.2. Monazite U-Pb age

Monazites from two thin sections of biotite quartz veins have been analyzed for U-Pb age by LA-ICP-MS, with the results presented in Table 2. The monazites from the two thin sections both show relatively high concentrations of U (610 to 2739 ppm) and Th (37573 to 172189 ppm) and variable common Pb (4.5 to 330 ppm). Thirty-four spots of the monazite from the 17T40 thin section obtain a Tera-Wasserburg U-Pb lower intercept age of 133.2 $\pm$ 1.7 Ma (2σ; MSWD = 0.77), and the ^{207}Pb corrected data yield a weighted mean ^{206}Pb/^{238}U age of 132.7 $\pm$ 1.1 Ma (2σ; MSWD = 0.92) (Fig. 8a-b). Seventeen spots of the monazite from the 17T34 thin section give a Tera-Wasserburg U-Pb lower intercept age of 134.8 $\pm$ 8.0 Ma (2σ; MSWD = 0.87), and the ^{207}Pb corrected data yield a weighted mean ^{206}Pb/^{238}U age of 134.2 $\pm$ 1.8 Ma (2σ; MSWD = 0.99) (Fig. 8c-d).

Table 1
LA-ICP-MS cassiterite U-Pb dating results of the Tiantangshan deposit.

	Th (ppm)	U (ppm)	Isotopic ratio							Age (Ma)		^{207}Pb corrected age (Ma)	
			^{207}Pb/^{206}Pb	1σ	^{207}Pb/^{235}U	1σ	^{206}Pb/^{238}U	1σ		^{206}Pb/^{238}U	1σ	^{206}Pb/^{238}U	1σ
Cst I													
1	0.02	53.52	0.053376	0.001582	0.151748	0.006294	0.020629	0.000156		131.6	3.8		
2	0.01	28.13	0.048953	0.001856	0.138912	0.006673	0.020590	0.000192		131.4	3.8		
3	0.00	15.15	0.051235	0.002713	0.150353	0.009238	0.021293	0.000291		135.8	4.2		
4	0.00	16.78	0.049939	0.002336	0.143826	0.008031	0.020898	0.000253		133.3	4.0		
5	0.00	37.72	0.047952	0.001570	0.138968	0.006102	0.021028	0.000178		134.2	3.9		
6	0.01	57.32	0.050085	0.001238	0.147619	0.005616	0.021386	0.000154		136.4	3.9		
7	0.00	31.46	0.050172	0.001809	0.146602	0.006815	0.021202	0.000185		135.3	3.9		
8	0.00	28.10	0.049875	0.001884	0.143464	0.006897	0.020871	0.000209		133.2	3.9		
9	0.00	46.56	0.049452	0.001321	0.142183	0.005623	0.020862	0.000170		133.1	3.8		
10	0.00	38.61	0.051196	0.001682	0.148348	0.006538	0.021025	0.000187		134.1	3.9		
11	0.00	85.93	0.048141	0.000959	0.139416	0.004879	0.021013	0.000139		134.1	3.8		
12	0.01	56.47	0.052420	0.001289	0.152067	0.005781	0.021049	0.000158		134.3	3.9		
13	0.00	29.76	0.050009	0.001647	0.146228	0.006473	0.021217	0.000202		135.3	4.0		
14	0.00	40.06	0.049371	0.001546	0.143342	0.006145	0.021067	0.000180		134.4	3.9		
15	0.00	17.84	0.047522	0.002456	0.136759	0.008224	0.020881	0.000265		133.2	4.1		
Cst II													
1	0.02	5.48	0.127574	0.008942	0.390676	0.030655	0.022220	0.000476				130.7	4.9
2	0.01	5.17	0.081205	0.006170	0.236554	0.019861	0.021137	0.000468				130.5	4.8
3	0.03	12.44	0.100007	0.003972	0.306539	0.015696	0.022241	0.000359				134.7	4.5
4	0.01	9.44	0.055659	0.003344	0.157829	0.010835	0.020575	0.000367				130.4	4.3
5	0.00	4.04	0.081691	0.007181	0.232064	0.022064	0.020612	0.000465				127.3	4.7
6	0.00	2.06	0.084891	0.011226	0.265174	0.037109	0.022665	0.000821				139.4	6.5
7	0.00	7.19	0.056133	0.004161	0.163117	0.013283	0.021085	0.000395				133.5	4.5
8	0.01	6.85	0.061572	0.004530	0.175166	0.014241	0.020643	0.000420				130.0	4.5
9	0.00	4.16	0.082318	0.010697	0.228086	0.030920	0.020105	0.000534				124.1	4.9
10	0.00	7.14	0.065148	0.005060	0.195804	0.016649	0.021808	0.000443				136.8	4.8
11	0.00	1.29	0.137387	0.022157	0.396011	0.067193	0.020915	0.000935				121.8	7.0
12	0.00	0.75	0.123274	0.019064	0.404820	0.067223	0.023828	0.001278				140.8	9.1
13	0.00	3.69	0.069032	0.006682	0.207322	0.021644	0.021792	0.000596				136.2	5.4
14	0.00	3.60	0.085256	0.008027	0.247522	0.025096	0.021066	0.000529				129.6	5.0
15	0.00	2.00	0.125585	0.013898	0.374277	0.044570	0.021625	0.000734				127.5	6.0
16	0.03	2.01	0.121504	0.010600	0.398658	0.038493	0.023807	0.000773				140.9	6.4
17	0.01	4.00	0.082432	0.007186	0.240182	0.022689	0.021142	0.000491				130.4	4.9
18	0.03	43.85	0.059567	0.001579	0.172742	0.006818	0.021042	0.000178				132.8	3.9
19	0.01	44.87	0.049094	0.001513	0.142785	0.006048	0.021103	0.000164				134.6	3.9
20	0.00	1.76	0.087774	0.012437	0.282466	0.042597	0.023350	0.001013				143.1	7.6
21	0.00	1.95	0.113909	0.013249	0.359870	0.044750	0.022923	0.000778				136.8	6.4
22	0.01	2.41	0.172284	0.023163	0.544939	0.077187	0.022951	0.000796				128.6	6.5
23	0.03	2.93	0.095259	0.009150	0.282550	0.029599	0.021522	0.000668				131.0	5.7
24	0.00	4.78	0.061785	0.005239	0.179747	0.016643	0.021109	0.000516				132.9	5.0
25	0.01	1.33	0.136260	0.015223	0.423483	0.052055	0.022551	0.000968				131.4	7.3
26	0.01	11.88	0.056070	0.003106	0.163131	0.010435	0.021111	0.000326				133.7	4.3
27	0.02	21.34	0.084673	0.003489	0.258731	0.013248	0.022172	0.000262				136.4	4.3
28	0.01	3.86	0.097608	0.008494	0.290793	0.027859	0.021617	0.000620				131.3	5.5
29	0.00	9.24	0.054400	0.003397	0.159527	0.011222	0.021278	0.000346				135.0	4.4
30	0.00	17.37	0.053118	0.002777	0.154540	0.009393	0.021110	0.000281				134.1	4.1
31	0.11	49.79	0.072986	0.001865	0.222122	0.008581	0.022082	0.000164				137.5	4.0
32	0.03	30.67	0.062765	0.001973	0.189605	0.008164	0.021919	0.000198				137.9	4.1
33	0.01	77.45	0.052348	0.001206	0.151638	0.005587	0.021019	0.000138				133.6	3.8
34	0.05	77.20	0.053557	0.001273	0.157103	0.005877	0.021285	0.000152				135.1	3.9

Fig. 7. LA-ICP-MS cassiterite U-Pb diagrams of the Tiantangshan deposit. Concordia diagram (a) and weighted mean age (b) of Cst I; Tera–Wasserburg concordia diagrams (c) and ^{207}Pb corrected weighted mean age (d) of Cst II.

5.3. Trace element of alteration rocks

Two samples of K-feldspar alteration and three samples of greisen were analyzed for whole-rock trace elements, with the results presented in Supplemental Table S1. The K-feldspar alteration and greisen rocks both show distinct tetrad chondrite-normalized REE patterns that are relatively enriched in La to Nd, and Er to Lu, but markedly depleted in Sm to Ho, particularly for Eu (Fig. 9a). Additionally, two greisen samples display negative Ce anomalies in the REE patterns (Fig. 9a). The K-feldspar alteration samples have distinctly high concentrations of Rb (1992–2092 ppm), whereas, the greisen samples are relatively depleted in Rb (110–501 ppm). The K-feldspar alteration samples have elemental ratio values of Zr/Hf (12.5–12.6), Nb/Ta (6.5–6.8), Y/Ho (15.9–17.0), and for the greisen samples, these values are 3.5–11.1, 3.6–5.7 and 11.9–14.9, respectively (Fig. 9b-c).

6. Discussion

6.1. Geochronological framework of the Tiantangshan deposit

The timing of Sn mineralization of the Tiantangshan deposit is estimated by U-Pb dating of hydrothermal cassiterite, that is the key tin-dominated mineral in the deposit. Shown by the LA-ICP-MS analytical results, the cassiterite contains several to dozens of ppm of U with relatively low common Pb. The closure temperature of cassiterite U-Pb system is revealed reaching up to 560 °C for 1 µm grain, and up to 860 °C for 1 mm grain (Zhang et al., 2011), which is commonly higher than granite solidus temperature and its crystallization temperature (ca. 300 to 400 °C). Such chemical characteristics and high isotopic closure temperature make cassiterite U-Pb dating an ideal and direct approach

for timing of Sn mineralization (e.g., Yuan et al., 2008; Zhang et al., 2017). It is noticed that two stages of cassiterite, including Cst I and Cst II, occur in the Tiantangshan deposit, that are distinct in color and micro-texture features (Fig. 3e, f). Our LA-ICP-MS analyses show that the Cst I and Cst II yield (^{207}Pb-corrected) weighted mean ^{206}Pb/^{238}U age of 133.9 ± 2.0 Ma (2σ) and 133.2 ± 1.6 Ma (2σ), respectively (Fig. 7), that are consistent within analytical error. Hence, the tin mineralization of the Tiantangshan deposit occurred at 134 to 133 Ma, and the two stages of cassiterite were formed under the same hydrothermal activity.

Monazite in biotite quartz veins is usually developed with local abundance, and commonly shows spatial association with hydrothermal minerals in the veins, like molybdenite, Bi-sulfide minerals and fluorite (Fig. 5e and f), which are indicative of its hydrothermal origin (Schandl and Gorton, 2004). Crucially, monazite is generally associated with biotite in the veins (Fig. 5f and g), and also distributed along quartz vein walls where hydrothermal biotite alteration of volcanic wall rocks occurred (Fig. 5e), which are suggestive of their intergrown relationship. Thus, the timing of Rb mineralization of the Tiantangshan deposit can be estimated by U-Pb dating of the monazite. Monazites from two thin sections of biotite quartz vein yield ^{207}Pb-corrected weighted mean ^{206}Pb/^{238}U ages of 134.2 ± 1.8 Ma (2σ) and 132.7 ± 1.1 Ma (2σ) (Fig. 8). The ages are comparative to the oldest age of the ^{40}Ar/^{39}Ar age of hydrothermal biotite by previous study (133.5–129.7 Ma; Jia, 2016). However, the closure temperature of biotite Ar-Ar system is relatively low (<350 °C; Harrison et al., 1985), and ^{40}Ar/^{39}Ar ages usually do not represent crystallization ages of minerals but are related to cooling history due to Ar diffusion at lower temperatures (Chiaradia et al., 2013). By contrast, monazite is robust in U-Th-Pb isotopic system with high closure temperature up to 750 °C (Harrison et al., 2002). Thus, the obtained monazite U-Pb ages in this study give a more accurate

Table 2
LA-ICP-MS monazite U-Pb dating results of the Tiantangshan deposit.

	Th (ppm)	U (ppm)	Isotopic ratio						^{207}Pb corrected age (Ma)	
			^{207}Pb/^{206}Pb	1σ	^{207}Pb/^{235}U	1σ	^{206}Pb/^{238}U	1σ	^{206}Pb/^{238}U	1σ
17 T40										
1	64,575	974	0.3604	0.0173	1.6700	0.1034	0.0332	0.0012	132.9	7.5
2	71,111	1854	0.1763	0.0126	0.6388	0.0581	0.0251	0.0008	135.9	4.8
3	85,676	1057	0.6463	0.0137	6.4204	0.1325	0.0724	0.0012	131.4	7.0
4	172,189	2739	0.5610	0.0112	4.2393	0.1273	0.0544	0.0011	134.1	6.6
5	103,051	1321	0.4657	0.0131	2.6019	0.0715	0.0407	0.0008	130.1	5.1
6	96,770	1009	0.4582	0.0122	2.6239	0.0699	0.0420	0.0008	136.4	5.1
7	82,846	976	0.4707	0.0161	2.6578	0.0882	0.0413	0.0011	130.4	6.8
8	65,154	1475	0.2195	0.0110	0.7808	0.0434	0.0256	0.0005	130.1	3.4
9	73,032	1579	0.1102	0.0065	0.3501	0.0198	0.0233	0.0004	137.7	2.5
10	66,554	1335	0.1497	0.0070	0.4937	0.0238	0.0240	0.0004	134.5	2.6
11	68,845	1175	0.1460	0.0066	0.4754	0.0223	0.0238	0.0005	134.4	3.1
12	56,318	1016	0.1814	0.0082	0.5917	0.0264	0.0240	0.0005	128.8	3.0
13	61,786	1077	0.1642	0.0072	0.5494	0.0242	0.0244	0.0004	134.2	2.6
14	91,446	2538	0.2104	0.0087	0.7817	0.0497	0.0261	0.0007	134.4	4.1
15	37,573	761	0.1538	0.0103	0.4924	0.0285	0.0241	0.0005	134.1	3.4
16	52,824	805	0.1430	0.0093	0.4413	0.0251	0.0229	0.0005	129.6	2.9
17	45,155	847	0.1561	0.0082	0.5138	0.0271	0.0240	0.0005	133.4	3.3
18	48,672	1176	0.1281	0.0059	0.3935	0.0170	0.0225	0.0004	129.8	2.7
19	46,912	851	0.1578	0.0089	0.5130	0.0262	0.0240	0.0005	133.2	3.0
20	52,336	963	0.1500	0.0063	0.5146	0.0226	0.0250	0.0005	139.8	3.2
21	47,830	887	0.1954	0.0083	0.7022	0.0271	0.0265	0.0005	139.5	3.4
22	45,597	1398	0.2696	0.0084	1.0180	0.0340	0.0275	0.0006	129.0	3.6
23	44,390	794	0.2246	0.0109	0.8206	0.0365	0.0269	0.0005	135.7	3.4
24	58,274	1355	0.1847	0.0071	0.6118	0.0234	0.0241	0.0004	128.9	2.5
25	54,382	1147	0.1987	0.0076	0.6841	0.0259	0.0251	0.0004	131.4	2.6
26	54,342	1175	0.4169	0.0121	2.2042	0.0767	0.0383	0.0008	136.8	5.3
27	39,482	610	0.2643	0.0139	0.9755	0.0404	0.0277	0.0007	131.0	4.2
28	75,988	1500	0.2173	0.0089	0.7890	0.0366	0.0261	0.0005	133.0	3.1
29	76,367	1354	0.1539	0.0074	0.4835	0.0205	0.0230	0.0005	128.5	3.0
30	76,018	1275	0.1498	0.0068	0.4808	0.0187	0.0238	0.0005	133.5	3.0
31	65,879	1031	0.1923	0.0082	0.6521	0.0263	0.0248	0.0004	131.2	2.8
32	86,647	1328	0.2113	0.0090	0.7468	0.0303	0.0259	0.0005	133.0	2.9
33	87,669	1366	0.1931	0.0067	0.6433	0.0199	0.0244	0.0004	128.8	2.6
34	57,417	918	0.1815	0.0078	0.6118	0.0238	0.0250	0.0006	133.9	3.5
17 T34										
1	58,235	1333	0.2115	0.0075	0.7456	0.0271	0.0265	0.0010	136.4	6.5
2	80,388	1510	0.2140	0.0090	0.7782	0.0328	0.0275	0.0011	140.8	7.0
3	78,791	1479	0.2383	0.0083	0.9301	0.0336	0.0284	0.0006	140.4	3.5
4	76,331	1332	0.2193	0.0090	0.7837	0.0309	0.0261	0.0005	132.8	3.2
5	66,035	1325	0.1835	0.0065	0.6468	0.0224	0.0259	0.0006	138.8	4.0
6	89,005	1549	0.2375	0.0079	0.9017	0.0317	0.0276	0.0006	136.6	3.8
7	77,190	2254	0.2378	0.0098	0.8763	0.0334	0.0270	0.0006	133.4	4.0
8	81,346	1463	0.2539	0.0086	0.9935	0.0323	0.0285	0.0005	137.5	3.3
9	75,130	1592	0.2489	0.0108	0.9228	0.0371	0.0271	0.0006	131.6	3.5
10	55,816	1584	0.2008	0.0079	0.6801	0.0249	0.0247	0.0005	129.3	3.0
11	75,619	1746	0.2422	0.0074	0.8942	0.0267	0.0268	0.0005	131.5	3.0
12	90,442	1452	0.3108	0.0088	1.3499	0.0354	0.0315	0.0005	138.4	3.4
13	74,907	1361	0.2785	0.0113	1.0952	0.0438	0.0284	0.0005	131.8	3.3
14	72,156	1278	0.2788	0.0108	1.0916	0.0348	0.0285	0.0005	132.3	3.4
15	82,575	1369	0.3445	0.0134	1.4653	0.0546	0.0310	0.0007	128.2	4.2
16	68,191	1758	0.2234	0.0103	0.8139	0.0310	0.0270	0.0007	136.6	4.4
17	78,861	1461	0.2352	0.0099	0.8700	0.0332	0.0270	0.0006	134.0	3.7

constraint on the timing of Rb mineralization of the Tiantangshan deposit.

The obtained U-Pb ages of cassiterite and monazite are consistent within analytical error (134 to 133 Ma), which suggests that both of the Sn and Rb mineralization of the Tiantangshan deposit were formed from the same hydrothermal activity. The mineralization ages are close to the zircon U-Pb age of the alkali feldspar granite (ca. 136 Ma; Peng et al., 2021; Fig. 10). The Sn and W mineralization of the Tiantangshan deposit are developed continuously from greisen, the hydrothermal product of fluid exsolution of the granite, suggesting their origin from the alkali feldspar granite. Meanwhile, the concentration of Ce decreases from the alkali feldspar granite, K-feldspar alteration to the greisen, with the latter showing marked negative Ce anomalies in chondrite-normalized REE partition pattern (Fig. 9a). The decreases in contents, particularly for the greisen, suggest that the Ce was significantly partitioned into

fluids with fluid exsolution, which is a necessary element of Ce for monazite of the biotite quartz veins. Therefore, the consistent ages combined with the chemical variations suggest that the polymetallic mineralization of the Tiantangshan deposit is genetically related to the alkali feldspar granite. Noticeably, the volcanic rocks, serving as the wall rocks of the granite and the related polymetallic mineralization, have consistent ages (ca. 137 Ma) with the alkali feldspar granite within analytical uncertainties (Fig. 10; Peng et al., 2021). The consistent ages suggest that the volcanic rocks and the alkali feldspar granite were likely formed from the same magmatic event. To sum up, a series of magmatic-hydrothermal events successively occurred in the Tiantangshan deposit, including volcanic eruptions (ca. 137 Ma), alkali feldspar granitic magmatism (ca. 136 Ma) and later Rb-Sn-W polymetallic mineralization (ca. 134 to 133 Ma) (Fig. 10).
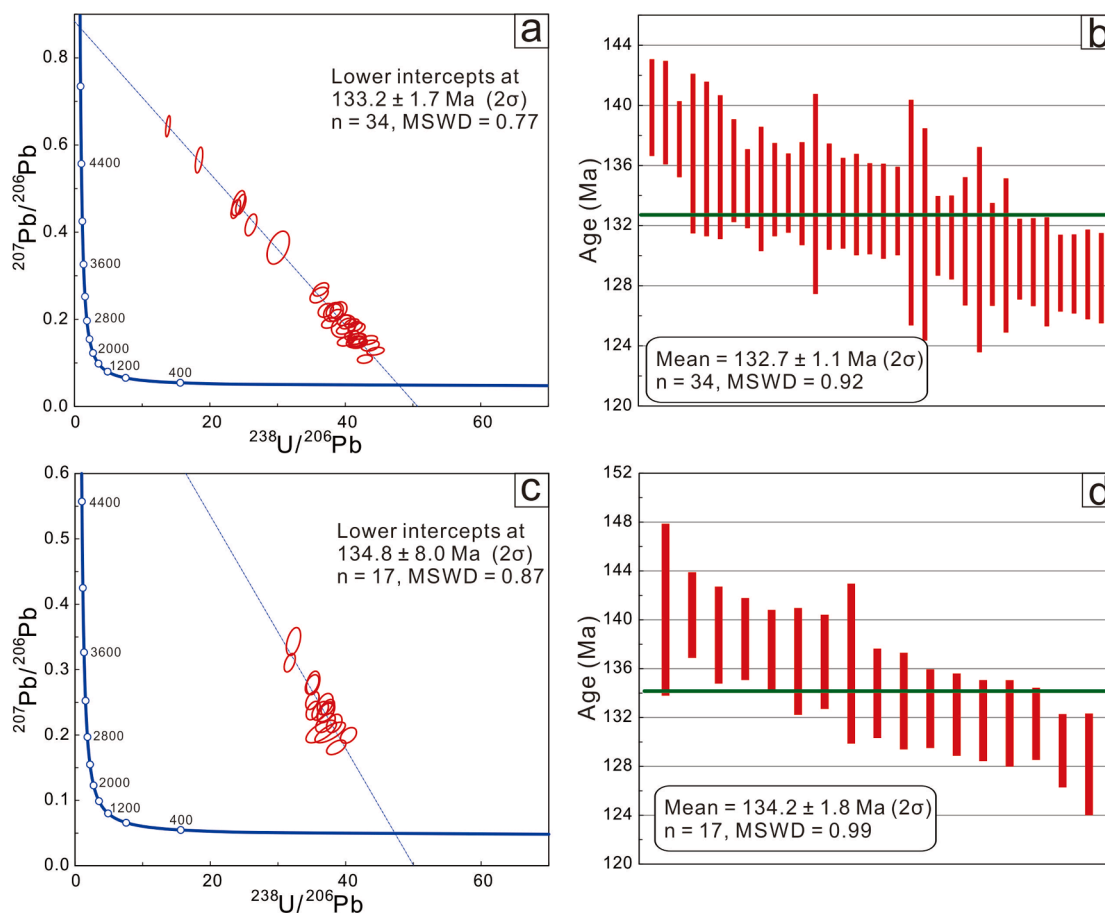
Fig. 8. LA-ICP-MS U-Pb diagrams of monazite from biotite quartz vein of the Tiantangshan deposit. Tera-Wasserburg concordia diagrams (a) and [207]Pb corrected weighted mean age (b) of 17T40 sample; Tera-Wasserburg concordia diagrams (c) and [207]Pb corrected weighted mean age (d) of 17T34 sample.

6.2. Genetic model of the Tiantangshan deposit

The ore-related alkali feldspar granite and the volcanic sequences at the Tiantangshan deposit show close temporal-spatial relations (Fig. 2c; Fig. 10), which implies a magma linkage between them. The granite is more silicic and evolved in composition and slightly more depleted in Nd-Hf isotopes than the volcanic rocks, and Peng et al. (2021) proposed that the granite was formed by extensive fractional crystallization of the parental magma of the volcanics, previously recharged by mantle-derived magma. The crystal mush model is commonly proposed to account for the magma connection between volcanic and intrusive rocks, in which, the former is formed by extracted melt from a crystal-rich magma chamber, and the remaining crystal mush solidify to form intrusive rocks (e.g., Bachmann et al., 2007; Cashman et al., 2017). Following the model, the volcanic rock is expected to be more silicic and evolved in composition than the intrusive one, which is just contrary to the Tiantangshan case. It is noteworthy that the intermediate-acid volcanic rocks at Tiantangshan are all rich in crystal phenocrysts, distinguished from the crystal-poor nature of the erupted highly evolved rhyolite in crystal mush model (e.g., Bachmann et al., 2007; Deering et al., 2016). In addition, recent studies also reported volcanic-intrusive complexes, where granitoids evolved to more fractionated composition than the coeval and cogenetic volcanic rocks, and similarly, the volcanic rocks were also characterized by crystal-rich nature (Cheng et al., 2018; Zhou et al., 2020). The eruption of crystal-rich magma might contribute to retainment of highly evolved residual melt within magma chamber, and meanwhile, could prevent significant loss of volatile component during volcanic eruptions (Parmigiani et al., 2016; Cheng et al., 2018). Crucially, the early crystal-rich magmatic eruption might also facilitate

the retainment and preliminary enrichment of Rb, Sn and W in the evolved residual melt, which might be a critical magmatic process for the polymetallic mineralization of the Tiantangshan deposit. We envisage that a magma chamber undergoing fractional crystallization existed at depth, and mixture of crystal and melt was intermittently erupted to form the volcanic rocks at first, and a portion of highly evolved residual melt was retained within the chamber, which was eventually extracted to form the alkali feldspar granite.

The Tiantangshan deposit comprises hydrothermal alterations from the alkali feldspar granite, which is successively hydrothermal altered outwards, and transforms into greisen, with K-feldspar alteration occurring intermediately (Fig. 2c). The K-feldspar alterations, characterized by high Rb concentrations (1992–2092 ppm), correspond to the minor Rb ore bodies developed within the granitic alteration zones of the deposit. In this type of mineralization, Rb was likely incorporated by substituting for K of the K-feldspar (Teertstra et al., 1998; Černý et al., 2003; Han et al., 2021), which is markedly different with the major Rb mineralization related to hydrothermal micas. It is noticed that, compared with the alkali feldspar granite, the K-feldspar alteration and greisen exhibit markedly different REE partition patterns with more notable tetrad effect, and meanwhile, their elemental ratio values of Zr/Hf, Nb/Ta and Y/Ho are substantially lower (Fig. 9). These chemical features are suggestive of an increasing importance of fluid in the final stage of the magma-fluid system (e.g., Bau, 1996; Irber, 1999; Monecke et al., 2011), and consequently, hydrothermal fluid was important in the formation of K-feldspar alteration and related Rb enrichment. By comparison, greisen rocks are with much lower Rb contents and lower elemental ratio values of Zr/Hf, Nb/Ta and Y/Ho (Supplemental Table S1; Fig. 9), which correspond to extensive Rb-rich fluid exsolution
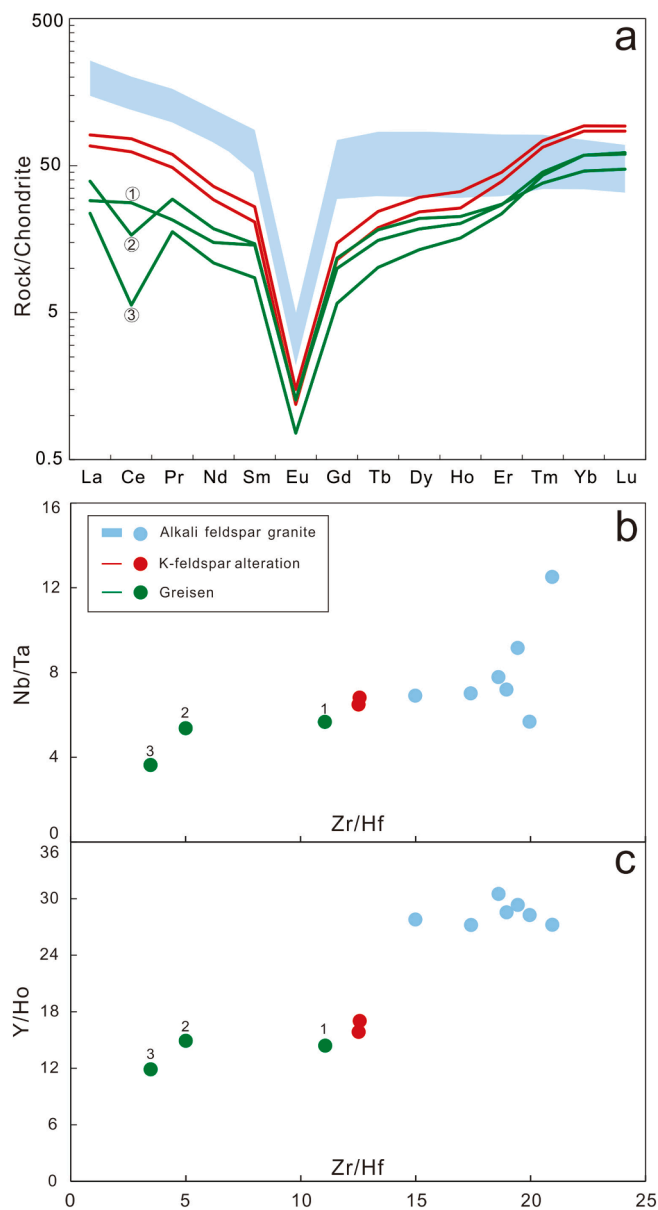
Fig. 9. Chondrite-normalized REE patterns (a), Nb/Ta vs. Zr/Hf (b) and Y/Ho vs. Zr/Hf (c) diagrams of the K-feldspar alteration rock and greisen of the Tiantangshan deposit. Data of the alkali feldspar are from Peng et al. (2021). Chondrite normalization values are from Sun and McDonough (1989).

and the formation of the hydrothermal quartz veins and the related Rb mineralization.

Three types of quartz veins, the ore bodies of the polymetallic mineralization, are developed outward from the greisen in the Tiantangshan deposit in response to fluid exsolution. The occurrence of the different quartz veins might imply a multi-stage evolution of ore-forming fluids occurred. However, the different quartz veins do not show evident cross cutting relationship, but are likely of spatially evolution relationship shown by their distribution (Fig. 2c). Noticeably, the wolframite-cassiterite quartz vein is largely comparative to the biotite quartz vein with respect to mineral paragenesis (Fig. 6). Magnetite, pyrite, native Bi and Bi-sulfides with minor arsenopyrite and little base metal minerals are superimposed in the wolframite-cassiterite quartz veins after wolframite and cassiterite, and analogously, the mineral assemblage are also developed in the biotite quartz veins, which are deposited later than the biotite, molybdenite and monazite (Fig. 6). In addition, by comparison, the ratio between native Bi and Bi-sulfides in the biotite quartz vein is lower than the wolframite-cassiterite quartz vein, which is likely reflective of decreased temperature and increased sulfur contents of fluids (Tooth et al., 2008). The comparability in mineral paragenesis suggests that a similar multi-stage evolution of ore-forming fluid occurred both in the wolframite-cassiterite quartz vein and biotite quartz vein, and therefore, the two quartz veins were connected in the fluid system, which is also supported by the consistent age of Sn and Rb mineralization obtained in this study. We deduce that different mineral assemblages were precipitated to form the different quartz veins in response to outward migration of fluids. The wolframite-cassiterite quartz vein was mainly formed in the contact zone between the greisen and volcanic wall rocks, while, with fluid migrating outwards, the biotite quartz veins were emplaced in the volcanic wall rocks. In addition, the developments of different quartz veins were also likely attributed to different fluid processes during the outward fluid migration. The extensive occurrence of biotite alteration of the wall rocks is suggestive of a critical role of fluid-rock interaction for the Rb mineralization during emplacement of biotite quartz vein. Whereas, for the wolframite-cassiterite quartz veins, other fluid processes were likely involved, like fluid cooling and/or boiling and/or mixing, commonly critical for W-Sn mineralization (e.g., Heinrich, 1990; Wood and Samson, 2000), which, however, needs further studies to clarify.

6.3. Implications for regional metallogenesis and geodynamic setting

South China is one of the most important Sn-W metallogenic province in the world, and in the past decades, a large number of precise geochronological data have demonstrated several episodes of Sn-W metallogenesis therein (e.g., Mao et al., 2013; Wang et al., 2020). The Nanling Range is one of the most important W-Sn belts located in the middle part of the South China, mainly including the southern Jiangxi, southern Hunan and northern Guangdong, and the numerous deposits were concentratedly formed during 160 to 150 Ma (Fig. 1; e.g., Mao et al., 2013; Yuan et al., 2019; Wang et al., 2020). Meanwhile, a Sn-dominated belt, represented by the giant Gejiu, Dachang and Dulong deposits, is located in the southwestern South China that covers the Guangxi province, eastern Yunnan and western Guangdong, in which, the numerous deposits were formed during late Cretaceous between 100
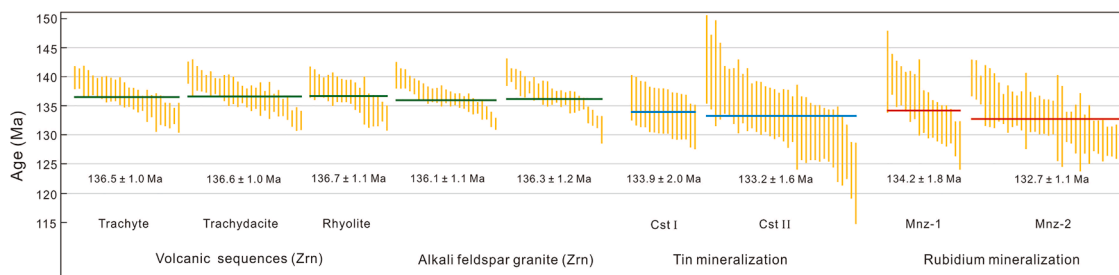

Fig. 10. Compilation of geochronological data (LA-ICP-MS U-Pb) for the volcanic rocks, alkali feldspar granite (from Peng et al., 2021) and the Sn and Rb mineralization (this study) of the Tiantangshan deposit.

and 75 Ma (Fig. 1; e.g., Guo et al., 2018; Cheng et al., 2019; Hu et al., 2021). From the temporal-spatial distribution of the W-Sn deposits, it was previously considered that the South China came to a relatively quiescent period for W-Sn mineralization during early Cretaceous. Recently, a W-dominated belt, represented by the giant Dahutang and Zhuxi deposits, was discovered, that is located in the Jiangnan orogen, including northern Jiangxi and southern Anhui, and the deposits therein were mainly formed during 150 to 125 Ma (Fig. 1; e.g., Huang and Jiang, 2014; Pan et al., 2017). Noticeably, recent studies also have recognized a new Sn-dominated belt located in the eastern Guangdong, i.e., the southeast coastal region of the South China, that mainly includes Xiling, Changpu, Taoxihu, Tashan, Jinkeng, Sanjiaowo and Houpoao, with a few W-dominated deposits of Lianhuashan and Feie'shan (Fig. 1). A series of cassiterite U-Pb, molybdenite Re-Os, mica Ar-Ar and zircon U-Pb isotopic dating have been carried out for the timing of Sn-W mineralization and associated magmatism of these deposits, which were constrained to be between 145 and 135 Ma (Fig. 11; Liu et al., 2017; Liu et al., 2018a; Liu et al., 2018b; Liu et al., 2018c; Qiu et al., 2017; Yan et al., 2018a; Yan et al., 2018b; Yan et al.,2020). The Tiantangshan deposit, situated in the northeastern Guangdong, has been revealed to be formed during 137 to 133 Ma in this study. Meanwhile, two Sn deposits of Yanbei and Taoxiba, located in southeastern Jiangxi, are revealed to be formed during early Cretaceous between ca. 140 and 130 Ma (Fig. 11; Liu, 2011; Li et al., 2018; Liu et al., 2021). Although Tiantangshan, Yanbei and Taoxiba are situated in the Nanling W-Sn belt, they are distinct by early Cretaceous mineralization, and moreover, their occurrences are inconsistent with the west-Sn and east-W distributions of the Nanling belt (Fig. 1). By contrast, these Sn deposits are of temporal relations and share similar mineralized features with the Sn-dominated belt in the eastern Guangdong (Fig. 11). We argue that Tiantangshan, Yanbei and Taoxiba are linked with the Sn deposits in the eastern Guangdong, which together forms a nearly N-S extending early Cretaceous Sn (±W) metallogenic belt.

One important geological feature for the Sn deposits from the southeastern belt is that polymetallic mineralization is commonly hosted by volcanic rocks (e.g., Liu et al., 2021). The volcanic-subvolcanic rocks of the Sn deposits from the southeast coast are genetically unrelated to the early Cretaceous Sn mineralization evidenced by their Jurassic ages (e.g., Liu et al., 2018c; Liu et al., 2021). However, unlike these deposits, the volcanic rocks and ore-related granitoids of the Tiantangshan, Yanbei and Taoxiba deposits are nearly coeval (Fig. 11; Liu, 2011; Li et al., 2018; Liu et al., 2021; Peng et al., 2021). Although there somewhat remains controversial on the magmatic linkage between the volcanic and intrusive rocks for the Yanbei and Taoxiba in the Huichang volcanic basin (Liu, 2011; Li et al., 2018), a volcanic-intrusive connection was revealed to be existed in the Tiantangshan deposit (Figs. 10 and 11; Peng et al., 2021). Similarly, Cheng et al. (2018)

introduced the Herberton Sn-W-Mo district in Queensland, Australia, where ore-related granitoids and Sn mineralization were genetically linked with coeval volcanic eruptions. These cases all point to a possible genetical relation between Sn-W mineralization and volcanic-subvolcanic rocks, and imply the exploration potential of Sn (±W)-rare metal deposit in volcanic basin. In the eastern Nanling Range, an inland volcanic basin belt is developed in the southern Jiangxi to northern Guangdong, which comprises three episodes of volcanic eruptions of early Jurassic (~190 Ma), early Cretaceous (~135 Ma), and late Cretaceous (~100 Ma) (Liu, 2018, and references therein). Considering the temporal-spatial distribution of Sn-W deposits in the South China, the early Cretaceous volcanic basins have more exploration potential for Sn (±W) and rare metal deposit, which include the Mabugang and Huichang volcanic basins.

The Yanshanian (Jurassic and Cretaceous) extensive magmatism and related large-scale W-Sn and rare metal metallogenesis in the Cathaysia block are commonly accepted to be related to the subduction of the paleo-Pacific plate (e.g., Zhou et al., 2006; Li and Li, 2007; Mao et al., 2013). During early Cretaceous, the Sn (±W) and rare metal mineralization in the Cathaysia block were mainly restricted in the southeastern coast region (Fig. 1). It is noticed that an early Cretaceous A-type belt of granite and volcanic rocks is developed in the Cathaysia block, and the southern part of which is spatially overlapped with the early Cretaceous Sn-dominated belt identified above (Peng et al., 2021). The ore-related granite of the Feie'shan, Sanjiaowo, Tiantangshan, Yanbei and Taoxiba were revealed to be of A-type affinities, and noticeably, the coeval volcanic rocks at the Tiantangshan are also with A-type chemical characteristics (Qiu et al., 2005; Li et al., 2018; Liu et al., 2018b; Yan et al., 2018a; Peng et al., 2021). The occurrences of A-type rocks are convincingly suggestive of extensional tectonic environment, regardless of their origin of magma source and petrogenetic models (e.g., Whalen et al., 1987; Eby, 1992). In addition, at the Tiantangshan, Yanbei and Taoxiba, the early Cretaceous volcanic eruptions, combined with possible magmatic linkages with the A-type granitoids, further point to an intensely extensional setting. For the early Cretaceous regional extension, numerous studies have related it with the roll back of the subducted paleo-Pacific plate, and Peng et al. (2021) introduced an asynchronous and asymmetric rollback during early Cretaceous beneath the Cathaysia block, inferred from the temporal-spatial distribution of A-type rocks.

7. Conclusions

(1) Precise LA-ICP-MS U-Pb dating of cassiterite and monazite reveal that the hydrothermal Sn and Rb mineralization of the Tiantangshan deposit occurred during 134 to 133 Ma. The ages indicate that the Rb-Sn-W polymetallic mineralization is
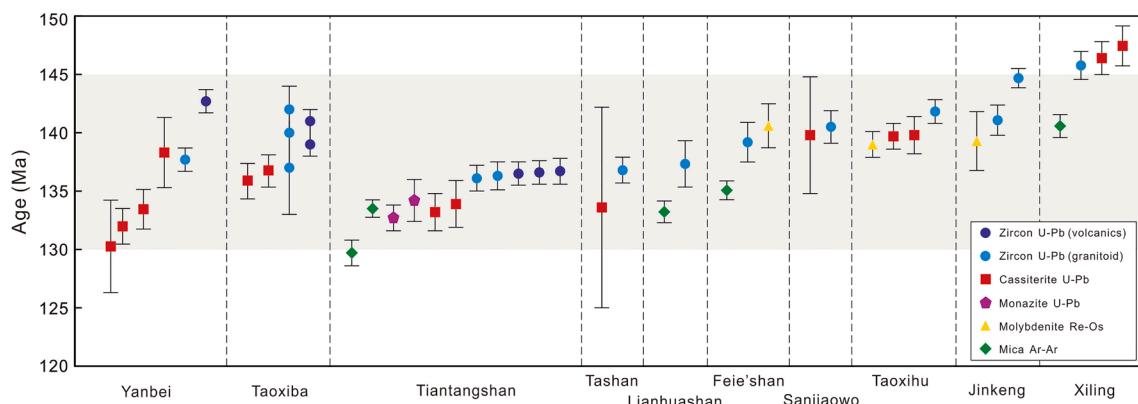

Fig. 11. Age compilation of magmatism and hydrothermal mineralization for deposits from the identified early Cretaceous Sn belt in Fig. 1. Data are from Liu et al., 2011; Qiu et al., 2017; Li et al., 2018; Liu et al., 2017; Liu et al., 2018a; Liu et al., 2018c; Liu et al., 2021; Yan et al., 2018a; Yan et al., 2018b; Yan et al., 2020.

genetically related to the alkali feldspar granite and a volcanic-intrusive connection at the deposit.

(2) The Rb-Sn-W polymetallic mineralization is present as different quartz veins, which are likely of spatial evolution relationship. The most of Rb resources of the deposit are hosted by hydrothermal biotite in the biotite quartz veins and related biotite alteration of volcanic wall rocks.

(3) K-feldspar alteration of the alkali feldspar granite hosts minor Rb resource of the deposit, and displays marked REE tetrad effect and low Zr/Hf, Nb/Ta and Y/Ho ratios, indicating an important involvement of hydrothermal fluids in this type of Rb enrichment.

(4) The Tiantangshan deposit (137 to 133 Ma) is largely coeval with the Yanbei, Taoxihu and the numerous Sn deposits in southeastern coast with respect to magmatism and mineralization. We propose these deposits delineate an early Cretaceous (145 to 130 Ma) Sn polymetallic metallogenic belt in the South China, which was likely formed under regional extension in response to roll back of the paleo-Pacific plate.

Declaration of Competing Interest

The authors declare that they have no known competing financial interests or personal relationships that could have appeared to influence the work reported in this paper.

Acknowledgements

Appendix A. Supplementary data

Supplementary data to this article can be found online at https://doi.org/10.1016/j.oregeorev.2021.104457.

References

Bachmann, O., Miller, C.F., de Silva, S.L., 2007. The volcanic–plutonic connection as a stage for understanding crustal magmatism. J. Volcanol. Geotherm. Res. 167 (1-4), 1–23.

Bau, M., 1996. Controls on the fractionation of isovalent trace elements in magmatic and aqueous systems: evidence from Y/Ho, Zr/Hf, and lanthanide tetrad effect. Contrib. Mineral. Petrol. 123 (3), 323–333.

Carr, P.A., Zink, S., Bennett, V.C., Norman, M.D., Amelin, Y., Blevin, P.L., 2020. A new method for U-Pb geochronology of cassiterite by ID-TIMS applied to the Mole Granite polymetallic system, eastern Australia. Chem. Geol. 539, 119539. https://doi.org/10.1016/j.chemgeo.2020.119539.

Cashman, K.V., Sparks, R.S.J., Blundy, J.D., 2017. Vertically extensive and unstable magmatic systems: a unified view of igneous processes. Science 355 (6331), eaag3055. https://doi.org/10.1126/science:aag3055.

Černý, P., Chapman, R., Teertstra, D.K., Novák, M., 2003. Rubidium- and cesium-dominant micas in granitic pegmatites. Am. Mineral. 88 (11-12), 1832–1835.

Chen, J., Lu, J.J., Chen, W.F., Wang, R.C., Ma, D.S., Zhu, J.C., Zhang, W.L., Ji, J.F., 2008. W-Sn-Nb-Ta-bearing granites in the Nanling Range and their relationship to metallogenesis. Geol. J. China Univ. 14, 459–473 (in Chinese with English abstract).

Cheng, Y., Spandler, C., Chang, Z., Clarke, G., 2018. Volcanic–plutonic connections and metal fertility of highly evolved magma systems: A case study from the Herberton Sn–W–Mo Mineral Field, Queensland. Australia. Earth Planet. Sci. Lett. 486, 84–93.

Cheng, Y.B., Spandler, C., Kemp, A., Mao, J.W., Rusk, B., Hu, Y., Blake, K., 2019. Controls on cassiterite (SnO$_2$) crystallization: Evidence from cathodoluminescence, trace-element chemistry, and geochronology at the Gejiu Tin District. Am. Mineral. 104, 118–129.

Chiaradia, M., Schaltegger, U., Spikings, R., Wotzlaw, J.-F., Ovtcharova, M., 2013. How accurately can we date the duration of magmatic-hydrothermal events in porphyry systems? —an invited paper. Econ. Geol. 108 (4), 565–584.

Deering, C.D., Keller, B., Schoene, B., Bachmann, O., Beane, R., Ovtcharova, M., 2016. Zircon record of the plutonic–volcanic connection and protracted rhyolite melt evolution. Geology 44 (4), 267–270.

Deng, J., Qiu, K.F., Wang, Q.F., Goldfarb, R., Yang, L.Q., Zi, J.W., Geng, J.Z., Ma, Y. 2020. In situ dating of hydrothermal monazite and implications for the geodynamic controls on ore formation in the Jiaodong gold province, eastern China. Econ. Geol. 115. 671–685.

Eby, G.N. 1992. Chemical subdivision of the A-type granitoids: petrogenetic and tectonic implications. Geology. 20. 641–644.

Guo, J., Zhang, R., Sun, W., Ling, M., Hu, Y., Wu, K., Luo, M., Zhang, L., 2018. Genesis of tin-dominant polymetallic deposits in the Dachang district, South China: insights from cassiterite U-Pb ages and trace element compositions. Ore Geol. Rev. 95, 863–879.

Guo, Y.Q. 2009. Study on geology and elemental chemistry of the Jinshizhang epithermal silver polymetallic deposit in northern Guangdong, China. Master thesis, China University of Geosciences (Beijing). 1–83 (in Chinese with English abstract).

Han, J., Chen, H., Hollings, P., Wang, J., Zhang, D., Zhang, L.e., Zeng, T.i., Ma, J., Ai, Y., 2021. Efficient enrichment of Rb during the magmatic-hydrothermal transition in a highly evolved granitic system: Implications from mica chemistry of the Tiantangshan Rb-Sn-W deposit. Chem. Geol. 560, 120020. https://doi.org/10.1016/j.chemgeo.2020.120020.

Harrison, T.M., Catlos, E.J., Montel, J.-M., 2002. U-Th-Pb dating of phosphate minerals. Rev. Mineral. Geochem. 48 (1), 524–558.

Harrison, T.M., Duncan, I., Mcdougall, I., 1985. Diffusion of Ar-40 in biotite: Temperature, pressure and compositional effects. Geochim. Cosmochim. Acta. 49, 2461–2468.

Heinrich, C.A. 1990. The Chemistry of Hydrothermal Tin(-Tungsten) Ore Deposition. Economic Geology 85. 457–481.

Hu, P.-C., Zhu, W.-G., Zhong, H., Zhang, R.-Q., Zhao, X.-Y., Mao, W., 2021. Late Cretaceous granitic magmatism and Sn mineralization in the giant Yinyan porphyry tin deposit, South China: constraints from zircon and cassiterite U-Pb and molybdenite Re–Os geochronology. Mineral. Deposita 56 (4), 743–765.

Huang, L.C., Jiang, S.Y., 2014. Highly fractionated S-type granites from the giant Dahutang tungsten deposit in Jiangnan Orogen, Southeast China: geochronology, petrogenesis and their relationship with W-mineralization. Lithos 202, 207–226.

Irber, W., 1999. The lanthanide tetrad effect and its correlation with K/Rb, Eu/Eu*, Sr/Eu, Y/Ho, and Zr/Hf of evolving peraluminous granite suites. Geochim. Cosmochim. Acta. 63 (3-4), 489–508.

Jia, H.X., 2016. Geological Geochemical Characteristics and Genesis of the Tiantangshan Tin Polymetallic Deposit, Longchuan County, Guangdong Province. Master Dissertation in. China University of Geosciences, Beijing, pp. 1–86.

Jia, R.-Y., Wang, G.-C., Geng, L., Pang, Z.-S., Jia, H.-X., Zhang, Z.-H., Chen, H., Liu, Z., 2019. Petrogenesis of the Early Cretaceous Tiantangshan A-Type Granite, Cathaysia Block, SE China: Implication for the Tin Mineralization. Minerals 9 (5), 257. https://doi.org/10.3390/min9050257.

Li, C.Y., Zhang, R.Q., Ding, X., Ling, M.X., Fan, W.M., Sun, W.D., 2016. Dating cassiterite using laser ablation ICP-MS. Ore Geol. Rev. 72, 313–322.

Li, Q., Zhao, K.-D., Lai, P.-C., Jiang, S.-Y., Chen, W., 2018. Petrogenesis of Cretaceous volcanic-intrusive complex from the giant Yanbei tin deposit, South China: implication for multiple magma sources, tin mineralization, and geodynamic setting. Lithos 296-299, 163–180.

Li, Z.-X., Li, X.-H., 2007. Formation of the 1300 km-wide intra-continental orogen and post orogenic magmatic province in Mesozoic South China: a flat-slab subduction model. Geology 35 (2), 179. https://doi.org/10.1130/G23193A.110.1130/2007041.

Liu, G.Q., 2018. Mesozoic volcanic basins and uranium mineralization in the eastern Nanling Range. Doctor thesis, China University of Geosciences 1–156 (in Chinese with English abstract).

Liu, P., Mao, J., Cheng, Y., Yao, W., Wang, X., Hao, D.i., 2017. An Early Cretaceous W-Sn deposit and its implications in southeast coastal metallogenic belt: Constraints from U-Pb, Re-Os, Ar-Ar geochronology at the Feie'shan W-Sn deposit. SE China. Ore Geol. Rev. 81, 112–122.

Liu, P., Mao, J., Lehmann, B., Peng, L., Zhang, R., Wang, F., Lu, G., Jiang, C., 2021. Cassiterite U-Pb dating of the lower Cretaceous Yanbei tin porphyry district in the Mikengshan volcanic basin. SE China. Ore Geol. Rev. 134, 104151. https://doi.org/10.1016/j.oregeorev.2021.104151.

Liu, P., Mao, J.W., Pirajno, F., Jia, L.H., Zhang, F., Li, Y., 2018a. Ore genesis and geodynamic setting of the Lianhuashan porphyry tungsten deposit, eastern Guangdong Province, SE China: constraints from muscovite 40Ar/39Ar and zircon dating and Hf isotopes. Mineral. Deposita 53, 797–814.

Liu, P., Mao, J., Santosh, M., Bao, Z., Zeng, X., Jia, L., 2018b. Geochronology and petrogenesis of the Early Cretaceous A-type granite from the Feie'shan W-Sn deposit in the eastern Guangdong Province, SE China: implications for W-Sn mineralization and geodynamic setting. Lithos 300-301, 330–347.

Liu, P., Mao, J.W., Santosh, M., Xu, L.G., Zhang, R.Q., Jia, L.H. 2018c. The Xiling Sn deposit, eastern Guangdong Province, Southeast China: a new genetic model from 40Ar/39Ar muscovite and U-Pb cassiterite and zircon geochronology. Econ. Geol. 113. 511–530.

Liu, Y., 2011. Characteristics of ore deposit geology and geochemisty, and ore genesis of the Taoxiba tin deposit in Huichang county, Jiangxi Province. MSc thesis, Beijing, China University of Geoscenices (in Chinese with English abstract).

Liu, Y.S., Hu, Z.C., Zong, K.Q., Gao, C.G., Gao, S., Xu, J., Chen, H.H. 2010. Reappraisement and refinement of zircon U-Pb isotope and trace element analyses by LA-ICP-MS. Chin. Sci. Bull. 55. 1535–1546.

Ludwig, K.R. 2012. Isoplot: A geochronological toolkit for Microsoft Excel. Special Publication no. 5, Berkeley Geochronology Center. 70.

Ma, W.-D., Fan, H.-R., Liu, X., Pirajno, F., Hu, F.-F., Yang, K.-F., Yang, Y.-H., Xu, W.-G., Jiang, P., 2017. Geochronological framework of the Xiadian gold deposit in the Jiaodong province, China: Implications for the timing of gold mineralization. Ore Geol. Rev. 86, 196–211.

Mao, J.W., Cheng, Y.B., Chen, M.H., Pirajno, F., 2013. Major types and time–space distribution of Mesozoic ore deposits in South China and their geodynamic settings. Mineral. Deposita 48 (3), 267–294.

Mao, J.W., Xie, G.Q., Guo, C.L., 2007. Large-scale tungsten mineralization in the Nanling region, South China: metallogenic ages and corresponding geodynamic processes. Acta Petrol. Sinica 23, 2329–2338 (in Chinese with English abstract).

Monecke, T., Kempe, U., Trinkler, M., Thomas, R., Dulski, P., Wagner, T. 2011. Unusual rare earth element fractionation in a tin-bearing magmatic-hydrothermal system. Geology 39. 295–298.

Ni, P., Wang, G.-G., Li, W.-S., Chi, Z., Li, S.-N., Gao, Y., 2021. A review of the Yanshanian ore-related felsic magmatism and tectonic settings in the Nanling W-Sn and Wuyi Au-Cu metallogenic belts, Cathaysia Block. South China. Ore Geol. Rev. 133, 104088. https://doi.org/10.1016/j.oregeorev.2021.104088.

Pan, X.F., Hou, Z.Q., Li, Y., Chen, G.H., Zhao, M., Zhang, T.F., Zhang, C., Wei, J., Kang, C., 2017. Dating the giant Zhuxi W-Cu deposit (Taqian-Fuchun Ore Belt) in South China using molybdenite Re-Os and muscovite Ar-Ar system. Ore Geol. Rev. 86, 719–733.

Parmigiani, A., Faroughi, S., Huber, C., Bachmann, O., Su, Y., 2016. Bubble accumulation and its role in the evolution of magma reservoirs in the upper crust. Nature 532 (7600), 492–495.

Peng, H.-W., Fan, H.-R., Jiang, P., Hu, H.-L., Lan, T.-G., 2021. Two-stage rollbacks of the paleo-Pacific plate beneath the Cathaysia block during Cretaceous: Insights from A-type granites and volcanic rocks. Gondwana Res. 97, 158–175.

Qiu, J.S., McInnes, B.I.A., Jiang, S.Y., Hu, J., 2005. Geochemistry of the Mikengshan pluton in Huichang Country, Jiangxi Province and new recognition about its genetic type. Geochimica 34, 20–32 (in Chinese with English abstract).

Qiu, Z., Yan, Q., Li, S., Wang, H.e., Tong, L., Zhang, R., Wei, X., Li, P., Wang, L., Bu, A.n., Yan, L., 2017. Highly fractionated Early Cretaceous I-type granites and related Sn polymetallic mineralization in the Jinkeng deposit, eastern Guangdong, SE China: Constraints from geochronology, geochemistry, and Hf isotopes. Ore Geol. Rev. 88, 718–738.

Rasmussen, B., Sheppard, S., Fletcher, I.R., 2006. Testing ore deposit models using in situ U-Pb geochronology of hydrothermal monazite: Paleoproterozoic gold mineralization in northern Australia. Geology 34, 77–80.

Saliba, M., Matsui, T., Domanski, K., Seo, J.-Y., Ummadisingu, A., Zakeeruddin, S.M., Correa-Baena, J.-P., Tress, W.R., Abate, A., Hagfeldt, A., Gratzel, M., 2016. Incorporation of rubidium cations into perovskite solar cells improves photovoltaic performance. Science 354 (6309), 206–209.

Schandl, E.S., Gorton, M.P. 2004. A textural and geochemical guide to the identification of hydrothermal monazite; criteria for selection of samples for dating epigenetic hydrothermal ore deposits. Econ. Geol. 99. 1027–1035.

Sun, S.S., McDonough, W.F., 1989. Chemical and isotopic systematics of oceanic basalts: implication for mantle composition and processes. Geol. Soc. Lond. Spec. Pub. 42, 313–345.

Sun, Y., Wang, D.H., Wang, C.H., Li, J.K., Zhao, Z., Wang, Y., Guo, W.M., 2019. Metallogenic regularity, new prospecting and guide direction of rubidium deposits in China. Acta Geol. Sinica 93, 1231–1244 (in Chinese with English abstract).

Tapster, S.R., Bright, J.W.G., 2020. High-precision ID-TIMS cassiterite U-Pb systematics using a low-contamination hydrothermal decomposition: implications for LA-ICP-MS and ore deposit geochronology. Geochronology 2, 425–441.

Teertstra, D.K., ·Cerný, .P., Hawthorne, .F.C., 1998. Rubidium feldspars in granitic pegmatites. Can. Mineral. 36, 483–496.

Tomascak, P.B., Krogstad, E.J., Walker, R.J., 1996. U-Pb monazite geochronology of granitic rocks from Maine: implications for late Paleozoic tectonics in the Northern Appalachians. J. Geol. 104, 185–195.

Tooth, B., Brugger, J., Ciobanu, C., Liu, W.H., 2008. Modeling of gold scavenging by bismuth melts coexisting with hydrothermal fluids. Geology 36, 815–818.

Wang, D.H., Fan, H., Wang, Y., He, H.H., Li, X.M., Liu, X.X., Sheng, J.F., Liang, T., 2020. Regional metallogeny of Tungsten-tin-polymetallic deposits in Nanling region. South China. Ore Geol. Rev. 120, 103305.

Whalen, J.B., Currie, K.L., Chappell, B.W., 1987. A-type granites: geochemical characteristics, discrimination and petrogenesis. Contrib. Mineral. Petrol. 95, 407–419.

Williams, M.L., Jercinovic, M.J., Hetherington, C.J., 2007. Microprobe monazite geochronology: understanding geologic processes by integrating composition and chronology. Annu. Rev. Earth Planet. Sci. 35, 137–175.

Wood, S.A., Samson, I.M., 2000. The hydrothermal geochemistry of tungsten in granitoid environments: I. Relative solubilities of ferberite and scheelite as a function of T, P, pH, and mNaCl. Econ. Geol. 95, 143–182.

Wu, J.H., Liu, F.Y., Liu, S., 2011. SHRIMP U-Pb Zircon age of late Mesozoic trachyte in Xiajiang-Guangfeng and Sannan (Quannan, Dingnan and Longnan)-Xunwu volcanic belts. Geol. Rev. 57, 125–132 (in Chinese with English abstract).

Yan, Q.H., Wang, H., Chi, G.X., 2020. Pulsed magmatic fluid releasing in the formation of the Taoxihu Sn polymetallic deposit, eastern Guangdong, SE China: Evidence from fluid inclusions, cassiterite U-Pb geochronology, and stable isotopes. Geol. Rev. 126, 103724.

Yan, Q.H., Wang, H., Qiu, Z.W., Wei, X.P., Li, P., Dong, R., Zhang, X.Y., Zhou, K.L., 2018a. Origin of Early Cretaceous A-type granite and related Sn mineralization in the Sanjiaowo deposit, eastern Guangdong, SE China and its tectonic implication. Ore Geol. Rev. 93, 60–80.

Yan, Q.H., Wang, H., Qiu, Z.W., Wang, M., Mu, S.L., Wang, L.M., Bu, A., Wang, S.M., Li, S.S., Wei, X.P., Li, P., 2018b. Zircon and Cassiterite U-Pb ages and Lu-Hf isotopic compositions of Tashan tin-bearing porphyry in Guangdong province, SE China and its geological significance. Geotectonica et Metallogenia 42, 718–731 (in Chinese with English abstract).

Yuan, S.D., Peng, J.T., Hu, R.Z., Li, H.M., Shen, N.P., Zhang, D.L., 2008. A precise U-Pb age of cassiterite from the Xianghualing tin-polymetallic deposit (Hunan, South China). Miner. Deposita 43, 375–382.

Yuan, S.D., Williams-Jones, A.E., Romer, R.L., Zhao, P.L., Mao, J.W., 2019. Protolith-related thermal controls on the decoupling of Sn and W in Sn-W metallogenic provinces: insights from the Nanling region. China. Econ. Geol. 114, 1005–1012.

Zhang, D.L., Peng, J.T., Hu, R.Z., Yuan, S.D., Zheng, D.S., 2011. The closure of U-Pb isotope system in cassiterite and its reliability for dating. Geol. Rev. 57, 549–554 (in Chinese with English abstract).

Zhang, R.Q., Lehmann, B., Seltmann, R., Sun, W.D., Li, C.Y., 2017. Cassiterite U-Pb geochronology constrains magmatic-hydrothermal evolution in complex evolved granite systems: the classic Erzgebirge tin province (Saxony and Bohemia). Geology 45, 1095–1098.

Zhao, G.C., Cawood, P.A., 2012. Precambrian geology of China. Precambrian Res. 222–223, 13–54.

Zhou, J.S., Yang, Z.S., Wang, Q., Zheng, Y.C., Hou, Z.Q., Wyman, D.A., 2020. Extraction of high-silica from an upper crustal mamma reservoir: insights from the Narusongduo magmatic system, Gangdese arc. Am. Mineral. 105, 1572–1584.

Zhou, X.M., Sun, T., Shen, W.Z., Shu, L.S., Niu, Y.L., 2006. Petrogenesis of Mesozoic granitoids and volcanic rocks in South China: a response to tectonic evolution. Episodes 29, 26–33.